J Physiol 602.10 (2024) pp 2315–2341

The Journal of Physiology

Cross-*strata* co-occurrence of ripples with theta-frequency oscillations in the hippocampus of foraging rats

Pavithraa Seenivasan, Reshma Basak and Rishikesh Narayanan

Cellular Neurophysiology Laboratory, Molecular Biophysics Unit, Indian Institute of Science, Bangalore, India

Handling Editors: Katalin Toth & Gareth Morris

The peer review history is available in the Supporting Information section of this article (https://doi.org/10.1113/JP284629#support-information-section).

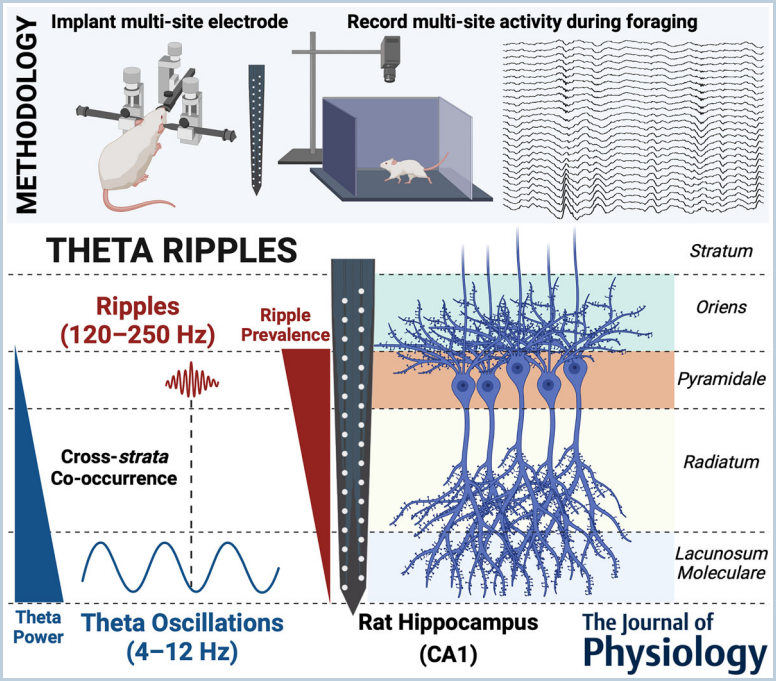

Abstract Brain rhythms have been postulated to play central roles in animal cognition. A prominently reported dichotomy of hippocampal rhythms links theta-frequency oscillations (4–12 Hz) and ripples (120–250 Hz) exclusively to preparatory and consummatory behaviours, respectively. However, because of the differential power expression of these two signals across hippocampal *strata*, such exclusivity requires validation through analyses of simultaneous

Pavithraa Seenivasan is a Biotechnology graduate from Sastra University in India. She then worked on research projects exploring non-linear dynamics in different biological systems such as the cardiac and uterine cells in the Institute of Mathematical Sciences in Chennai, India. Following that, she carried out her PhD in the Cellular Neurophysiology Laboratory at the Indian Institute of Science, Bangalore with Professor Rishikesh Narayanan. In her PhD, she studied the intrinsic properties of hippocampal neurons that contribute to efficient encoding of space in the brain. She also recorded extracellular signals from the hippocampus of foraging rats and explored the co-occurrence of two prominent oscillations that have been typically associated with distinct behavioural states. She is currently a postdoctoral fellow at the Janelia Research Campus (Ashburn, VA, USA), studying neurons involved in visual learning in fruit flies.

This article was first published as a preprint. Seenivasan P, Basak R, Narayanan R. 2022. Cross-strata co-occurrence of ripples with theta-frequency oscillations in the hippocampus of foraging rats. bioRxiv. https://doi.org/10.1101/2022.11.15.516579

DOI: 10.1113/JP284629

multi-*strata* recordings. We assessed co-occurrence of theta-frequency oscillations with ripples in multi-channel recordings of extracellular potentials across hippocampal *strata* from foraging rats. We detected all ripple events from an identified *stratum pyramidale* (SP) channel. We then defined theta epochs based on theta oscillations detected from the *stratum lacunosum-moleculare* (SLM) or the *stratum radiatum* (SR). We found ∼20% of ripple events (in SP) to co-occur with theta epochs identified from SR/SLM channels, defined here as theta ripples. Strikingly, when theta epochs were instead identified from the SP channel, such co-occurrences were significantly reduced because of a progressive reduction in theta power along the SLM-SR-SP axis. Behaviourally, we found most theta ripples to occur during immobile periods, with comparable theta power during exploratory and immobile theta epochs. Furthermore, the progressive reduction in theta power along the SLM-SR-SP axis was common to exploratory and immobile periods. Finally, we found a strong theta-phase preference of theta ripples within the fourth quadrant $[3\pi/2 - 2\pi]$ of the associated theta oscillation. The prevalence of theta ripples expands the potential roles of ripple-frequency oscillations to span the continuum of encoding, retrieval and consolidation, achieved through interactions with theta oscillations.

(Received 2 March 2023; accepted after revision 4 April 2024; first published online 24 April 2024)
Corresponding author R. Narayanan: Cellular Neurophysiology Laboratory, Molecular Biophysics Unit, Indian Institute of Science, Bangalore 560012, India. Email: rishi@iisc.ac.in

Abstract figure legend There are several lines of evidence from the rodent hippocampus that theta frequency oscillations (4–12 Hz) are rich in distal *strata*, while ripples (120–250 Hz) are prominent in *strata* that are within and around the pyramidal cell layer. Our goal here was to explore possible co-occurrence of these distinct bands of signals with differential distribution across *strata*. We simultaneously recorded extracellular signals from multiple *strata* in the hippocampus of foraging rats using multi-site silicon polytrodes. We identified theta epochs from extracellular signals recorded from distal *strata* and detected ripples from signals recorded through electrode sites closer to the pyramidal cell layer. We found ∼20% of ripple events to be nested within a stream of theta oscillations. We referred to such ripples that co-occurred with theta oscillations as theta-ripples. We found that theta ripples occurred preferentially during the fourth quadrant of the associated theta oscillation.

Key points

- The brain manifests oscillations in recorded electrical potentials, with different frequencies of oscillation associated with distinct behavioural states.
- A prominently reported dichotomy assigns theta-frequency oscillations (4–12 Hz) and ripples (120–250 Hz) recorded in the hippocampus to be exclusively associated with preparatory and consummatory behaviours, respectively.
- Our multi-*strata* recordings from the rodent hippocampus coupled with cross-*strata* analyses provide direct quantitative evidence for the occurrence of ripple events nested within theta oscillations.
- These results highlight the need for an analysis pipeline that explicitly accounts for the specific *strata* where individual oscillatory power is high, in analysing simultaneously recorded data from multiple *strata*.
- Our observations open avenues for investigations involving cross-*strata* interactions between theta oscillations and ripples across different behavioural states.

Introduction

Historically guided by single *stratum* recordings, a strong narrative has driven a dichotomy in the expression of theta-frequency oscillations and ripples in the rodent hippocampus. Specifically, from a behavioural perspective, theta oscillations (4–10 Hz) are associated with exploration or active engagement with external stimuli. In contrast, ripple events (120–250 Hz) embedded within sharp wave ripple (SPW-R) complexes have been observed during slow wave sleep or wakeful immobility. In addition to this behavioural dichotomy, theta oscillations

are implicated in encoding phenomena whereas ripples are associated with memory consolidation and retrieval. The exclusive nature of this dichotomy, in terms of the two distinct oscillatory bands being involved in behavioural and physiological processes, provides a compelling narrative for how electrical signals drive memory processes (Buzsaki, 1989, 2002; Buzsaki, 2015; Colgin, 2013; Girardeau & Lopes-Dos-Santos, 2021; Girardeau & Zugaro, 2011; Hasselmo & Stern, 2014; Joo & Frank, 2018; Klausberger et al., 2003; Roumis & Frank, 2015). In the present study, we systematically assessed this dichotomy using simultaneous multi-*strata* recordings from hippocampal CA1 of foraging rats, specifically asking if the occurrence of theta-frequency oscillations and ripples are indeed mutually exclusive in the recorded local field potentials (LFP).

Our rationale for revisiting the dichotomy and probing co-occurrences of theta- and ripple-frequency oscillations is three-fold. First, there are strong lines of evidence in the literature that the power distribution of theta-frequency oscillations and ripples are differential across different *strata* of the CA1 subregion (Buzsaki, 2002; Buzsáki, 2015; Gordon et al., 2005; Navas-Olive et al., 2022; Zutshi et al., 2022). Theta-frequency oscillations are prominent in the *stratum lacunosum-moleculare* (SLM) and the distal *stratum radiatum* (SR), whereas ripples are rich within the *stratum pyramidale* (SP). From an experimental design perspective, the differential power distribution of these two signals (theta-frequency oscillations and ripples) implies that their co-occurrence should not be assessed with single *stratum* recordings, but with simultaneous multi-*strata* recordings that span the SLM, SR and SP. From an analysis standpoint, this differential distribution requires that the two signals are detected from the *stratum* where their respective powers are higher. In other words, to analyse co-occurrence of these two oscillatory patterns, it is essential that ripples are detected from the SP LFP and theta oscillations are identified from the SLM/SR LFP. The differential power distribution implies that detection of ripples from SLM/SR or theta oscillations from the SP would result in lower numbers of both identified oscillatory patterns, thus providing a false dichotomy for their exclusive expression. Therefore, we hypothesized that several co-occurrences of theta oscillations with ripples in simultaneous multi-*strata* recordings would manifest if each oscillatory band were identified from the *strata* where they express with the highest power. Testing this hypothesis necessitated simultaneous acquisition of extracellular signals across multiple *strata* coupled with an analysis pipeline that identifies theta oscillations and ripples from the *stratum* where their power is known to be high.

Second, there are some pointers in the literature that suggest the possibility of ripples co-occurring with theta rhythm during REM sleep (e.g. Fig. 5 in Buzsáki, 2015), as well as during exploratory periods (O'Neill et al., 2006). However, these studies did not investigate ripples from the perspective of their cross-*strata* temporal coexistence with theta oscillations. Finally, there are lines of evidence for a shared role for plateau potentials (consequent to strong dendritic depolarization) during theta oscillations as well as in driving sharp waves in the CA1 subregion (Bittner et al., 2015; Bittner et al., 2017; Buzsaki, 2015; Buzsáki & Vanderwolf, 1983; Epsztein et al., 2011; Kamondi, Acsady, Buzsáki et al., 1998; McKenzie et al., 2021; Milstein et al., 2021; Zhao et al., 2020). This shared cellular signature provided us a further motivation to assess the potential co-occurrence of ripples with theta oscillations.

Motivated by these observations, we systematically assessed the hypothesis that theta oscillations and ripples might co-occur across hippocampal CA1 *strata*, given the established *stratum*-dependent expression profiles of LFPs in these two oscillatory bands. In testing the hypothesis, we introduced important changes to the experimental design and analyses pipeline to explicitly account for these differential expression profiles. First, we simultaneously recorded extracellular signals from multiple *strata* using silicon polytrodes in awake behaving animals, rather than restricting our attention to one specific *stratum*. Second, we independently analysed electrophysiological and behavioural data instead of making strong assumptions about the occurrence of specific bands of oscillations during specific behaviour. In doing this, we placed tight constraints (with reference to frequency and durations) on the identification of ripples and theta epochs, as well as on the delineation of immobile *vs*. exploratory periods of behaviour (with reference to velocity and durations). Third, and most importantly, we chose different *strata* for analysing theta oscillations and ripples, explicitly based on established knowledge about where the powers of these two oscillatory bands are maximal. Specifically, we chose the SP for identifying ripples and the SLM/SR for delineating theta epochs. We then assessed the cross-*strata* co-occurrence of theta oscillations and ripples using these simultaneously recorded LFP waveforms.

Our experimental design and analysis pipeline that accounted for differential expression profiles unveiled the existence of theta ripples, defined as ripples in the SP that co-occurred with theta oscillations in the SLM/SR. Around 20% of all detected ripples were theta ripples and occurred predominantly during immobile periods of foraging rats. All characteristics of theta ripples were comparable with those ripples that occurred in the absence of theta oscillations. Furthermore, the power of theta oscillations in the immediate vicinity of theta ripples was similar to theta power across identified theta epochs, together validating the identification process of theta ripples. Importantly, our analyses showed that theta oscillations observed during immobile and exploratory

periods were comparable in their power across *strata*, with a *stratum*-dependent reduction in the theta along the SLM-SR-SP-SO (SO stands for *stratum oriens*) axis for both periods. As a final test of our hypothesis, we used different channels along the SLM-SR-SP-SO axis to identify theta epochs to count the number of SP ripples counted as theta ripples when each of these channels were used as theta channels. We found a significant reduction in the number of identified theta ripples when SP or SO channel was chosen as the theta channel, compared to when SLM was the theta channel.

The present study demonstrates that the differential power profile stipulates simultaneous multi-*strata* recordings and advocates for the use of different *strata* for identifying theta oscillations and ripples, explicitly based on where their power is maximal. Deviations from the *strata* where these signals of two different frequencies have their highest power do not account for the differential spatial expression and result in missing co-occurrences of these two oscillations. Together, we argue that the prevalent dichotomy about the manifestation of theta-frequency oscillations and ripples should be reevaluated, after explicitly accounting for the differential *stratum*-dependent expression of these two oscillatory patterns. The prevalence of theta ripples expands the potential roles of ripple-frequency oscillations to span the continuum of encoding, retrieval and consolidation, achieved through interactions with theta oscillations.

Methods

Ethical approval

All experimental procedures were approved by the Institutional Animal Ethics Committee of the Indian Institute of Science, Bangalore (Approval number: CAF/Ethics/545/2017). All animals were procured from the institutional central animal facility at the Indian Institute of Science, Bangalore.

Surgical procedures

Male Sprague–Dawley (SD) rats of 6–8 months age were entrained to a 14:10 h light/dark photocycle for at least 2 weeks prior to surgery and were housed one per cage before and after surgery. They were provided *ad libitum* food and water, with the housing temperature maintained between 21° C and 23° C.

Animals were anaesthetized with gaseous isoflurane throughout the course of surgery and craniotomies were performed with a stereotaxic apparatus (963LS; David Kopf Instruments, Los Angeles, CA, USA). The co-ordinates for craniotomy were fixed at 3.5 mm along the anteroposterior (AP) axis from the bregma and 2.2 mm mediolaterally (ML) from the central axis. Silicon probes, specifically, polytrodes, with 32 contact points and a high spatial resolution of 25 μm spacing between the contact points (A1×32-Poly2; Neuronexus Inc., Ann Arbor, MI, USA) were lowered ∼3 mm dorsoventrally (DV) from the surface of the brain, following durectomy to reach the dorsal hippocampal CA1 (Fig. 1). The lowering process was performed at a rate of ∼1 μm s^{-1} to minimize probe and tissue damage as well as to facilitate smooth implantation. The craniotomy was then sealed with sterile bone wax. Six screws were drilled through the skull prior to craniotomy, to stabilize and strengthen the implant, two of which in the cerebellum served as ground and reference electrodes. The exposed skull area was then built up with dental cement all the way from the skull surface up to the base of the probe to provide stability and long-term retention of the implant.

Electrophysiological and behavioural acquisition

The rats were allowed to recover for about a week following surgery, during which they were gentled and habituated to the experimenter, recording room and acquisition cables. Recordings began the following week, during which extracellular field potentials were recorded from the hippocampus when the rats were engaged in a foraging behaviour. These extracellular potentials were acquired using a Neuralynx acquisition system (Neuralynx, Bozeman, MT, USA) at a sampling rate of 32 kHz and with a band pass frequency range of 0.1–6 kHz.

Behaviour involved exploration and foraging in an open cardboard box (59 × 49 × 47 cm) (Fig. 1*A*). The box was lined with cling film on the inside and a copper mesh on the outside (Fig. 1*A*). The interior plastic lining facilitated cleaning the arena walls and minimized the retention of olfactory cues. The exterior copper mesh which was grounded to a thick copper plate served as a Faraday cage to reduce external electromagnetic interference. Rats foraged in three kinds of arenas, distinguished from each other by three differently textured mats fixed as the floor of the arena. On a given day, animals foraged in two different arenas with three consecutive sessions in each arena, resulting in a total of six sessions per day. Each recording session lasted for a duration of 15–35 min and a total of 6 days of recordings were performed for each rat, thus giving a total of 36 sessions per rat. Four pieces of sweet biscuits (threptin diskettes, weighing ∼0.1 g) were manually pre-placed in random locations within the arena by the experimenter. The recording box that was lined with plastic on the inside was ethanol-wiped and cleaned between arena switches (once every three sessions), whereas the arena mats were washed following a consecutive three-session usage. Recordings

were consistently performed around the same time on any day, during their active time in complete darkness. Behavioural recordings were also performed in a linear maze set up for two rats (Rats 2 and 3). This consisted of a rectangular, laminated wooden box (98 × 17 × 24 cm). Each rat had 2 days of recordings in the linear maze, with three sessions (15–20 min per session) per day separated by a 5 min break between sessions.

Behavioural data was captured in the dark as video frames at a sampling rate of 60 frames per second, using a camera (PlayStation 3 eye, 99 028; Sony Corp., Tokyo, Japan) that was positioned on top of the arena. The visual programming language Bonsai (https://bonsai-rx.org/; Lopes et al., 2015) was used to set up the behavioural recording pipeline and served as an interface between the electrophysiological and behavioural acquisition. We employed custom-written programs in Bonsai to identify the LED headlight attached to the Neuralynx headstage, against a dark background based on colour thresholding. This allowed us to track the centroid of the LED as a function of time and to obtain the trajectory of the rat through each session of recording. We employed Bonsai to communicate with the camera as an input device connected to the computer while it connected with

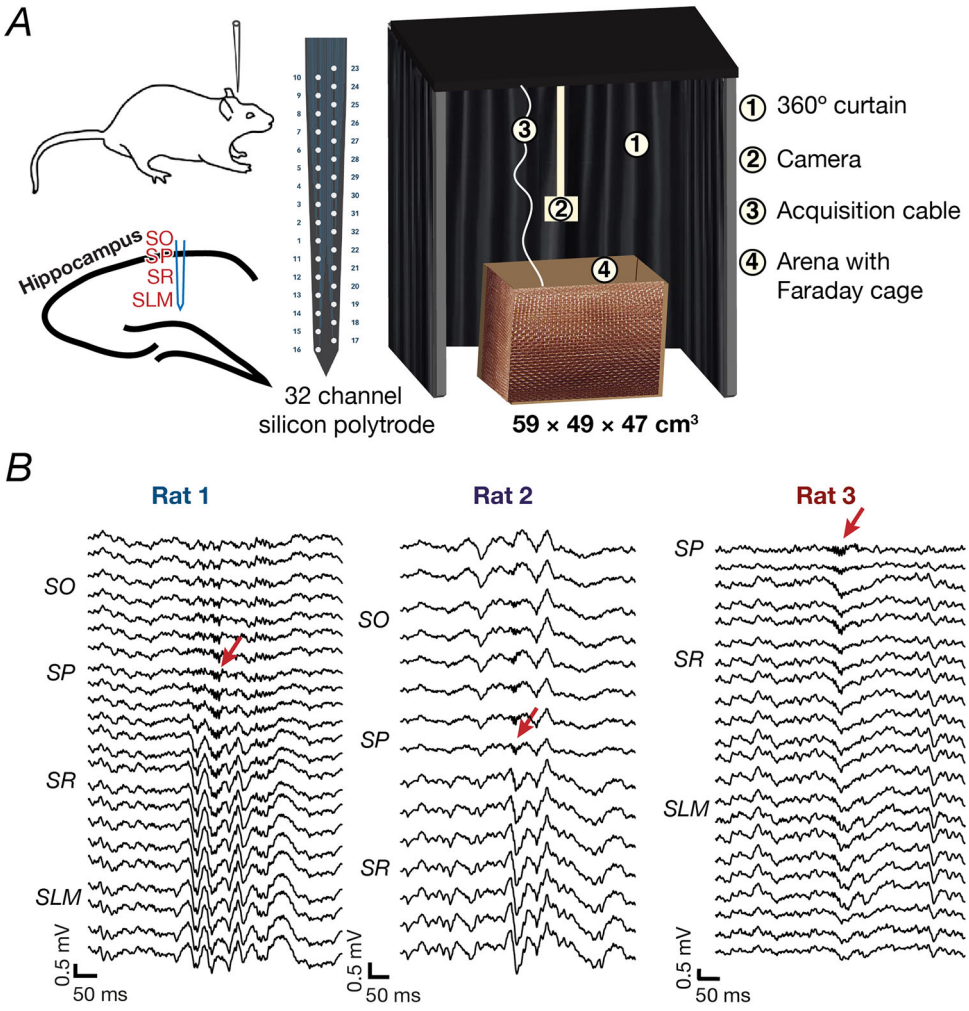

Figure 1. Electrode details, behavioral setup and laminar profiles
A, left: stereotaxis apparatus was used to implant electrodes into the dorsal hippocampus such that the silicon polytrode spans the different *strata* of the CA1 region. SO: *stratum oriens*. SP: *stratum pyramidale*. SR: *stratum radiatum*. SLM: *stratum lacunosum-moleculare*. Middle: pictorial representation of the 32 channel silicon polytrode employed for recordings. The numbers correspond to the order of the channels. Right: behavioural setup. The arena was a cardboard box. Behavioural recordings were performed by a ceiling-mounted camera. The entire setup was enclosed within black curtains spanning all sides. *B*, laminar profiles showing the local field potentials (0.5–300 Hz) recorded in all non-noisy channels from the three rats (left to right). The identity of the *strata* is specified on the left of the laminar profile. Ripples were localized within the SP (marked with a red arrow) and sharp waves are detected within the SR–SLM region. [Colour figure can be viewed at wileyonlinelibrary.com]

Neuralynx through a digital output signal that was sent through Arduino (https://www.arduino.cc). A record of the timing of this digital output signal from the camera was saved along with the electrophysiological data in Neuralynx, along with the positional information from the camera. This common origin time aided in referencing the two clocks towards synchronizing electrophysiology with behaviour during offline analyses.

Preprocessing of raw signals

All analyses of the acquired extracellular field recordings were performed using custom-written script within the FMA toolbox (https://fmatoolbox.sourceforge.net). Raw signals, sampled at 32 kHz, were decimated to 4 kHz and filtered between 0.5–300 Hz using a zero phase Butterworth filter of order 4, to derive local field potentials (LFP). Movement and grooming artifacts in the signal were identified as fluctuations that exceeded 5 standard deviations of the baseline signal and were removed. The removal of movement and grooming artifacts was performed by applying the 5 SD threshold on the LFP signals spanning 0.5–300 Hz, before additional filtering was used to identify specific bands of oscillations.

Identification of hippocampal *strata*

The various hippocampal CA1 *strata* – *stratum oriens* (SO), *stratum pyramidale* (SP), *stratum radiatum* (SR), and *stratum lacunosum-moleculare* (SLM) – were identified using multiple strategies. First, we used histological verification to infer the approximate location of the 800 μm silicon probe in the hippocampus of all rats. Second, we assessed the laminar profiles of LFP (0.5–300 Hz) signals to identify *strata* using well-established *strata*-specific characteristic signatures (Fig. 1*B*). To elaborate, sharp waves and ripples that are part of sharp wave ripple (SPW-R) complexes are known to spatially localize themselves within distinct CA1 *strata*. Specifically, ripples express within the SP layer, whereas sharp waves are observed in the SR layer of the CA1 (Buzsáki, 2015; Gordon et al., 2005; Mizuseki et al., 2011; Navas-Olive et al., 2022). We therefore marked the channel with maximal number of ripples as the SP and that with prominent sharp waves as the SR layer. Additionally, the SR-SLM band was identified by virtue of enhanced power in the theta frequency (6–10 Hz) band, the ordered organization of CA1 *strata* as SO-SP-SR-SLM (Andersen et al., 2006; Buzsaki, 2002) and the fixed distances between recording channels in our electrode (25 μm). SO was marked to include channels 100–150 μm above SP. Third, we confirmed *strata* identification through phase shifts observed in theta oscillations across different channels. In accordance with the characteristic phase inversion that occurs from SO to SLM (Buzsaki, 2002), we noted that the phase of the recorded signals reversed close to the identified SP layer across all three rats. Thus, a combination of these different strategies (histology data, ripple numbers, sharp wave location, theta power, known SO-SP-SR-SLM distances, phase shift), even in scenarios where part of the SP or SLM were unavailable as a result of electrode locations, allowed us to identify different *strata* across all three rats.

Detection of theta epochs and ripple events

Theta epochs were detected using instantaneous power within the theta frequency band (default 6–10 Hz) computed through multi-taper spectral estimation (Thomson, 1982). They were identified as segments of the recorded voltage signal where power in the theta frequency band exceeded 1 SD above mean. To enforce strictness in the identification of theta epochs, the minimum duration necessary for detection as a theta epoch was fixed to be 1 s. Analyses with different procedures for identifying theta epochs were employed to enable further corroboration of our results (Table 1).

To detect ripple events, the LFP signals recorded from all the channels were band-pass filtered in the ripple frequency range (120–250 Hz) using a zero-phase Butterworth filter of order 4. This filtered signal was subjected to ripple identification criteria. Specifically, the beginning and the end of a ripple were detected based on instances of ripple power exceeding 2 SD above mean and the peak of the ripple was identified by a 5 SD deflection above mean. Although the 5 SD deflection was identical to the threshold used in the pre-processing step for removing grooming and movement artifacts, the threshold values here involve SD on the ripple-filtered (120–250 Hz) signals whereas the preprocessing step involved SD on the LFP signal spanning 0.5–300 Hz. The minimum and maximum durations of ripple events were constrained to be within 20 and 200 ms, respectively, and the minimum inter-ripple interval was required to be at 30 ms. The entire ripple identification procedure was independently applied to all the channels initially, to identify *strata* and to eliminate events detected across many channels that are probably artifacts. Specifically, after detecting ripple-like events in all the recorded channels, putative ripple events in the SP layer were discarded if there were events detected in at least 10 channels, within 10 ms on either side of the ripple under consideration. These events, as a result of their simultaneous detection across channels, are probably related to movement or muscle related artifacts and not real ripples. The threshold number of 10 was arrived at by trial-and-error, balancing between

Table 1. Controls for computing theta ripple co-occurrences

Parameter changed	# Theta ripples	# Exploratory, theta ripples	# Immobile, theta ripples
RAT #1			
Default	444	24	312
Maze type (linear maze)	–	–	–
Theta frequency range ([4–10] Hz)	607	18	498
Velocity threshold (4,4)	444	39	303
Velocity threshold (6,6)	444	18	313
Velocity threshold (8,8)	444	6	316
Ripple validation (# channels: 12)	444	39	303
Theta detection (low level)	915	31	664
Theta detection (medium level)	204	14	145
RAT #2			
Default	2430	0	2261
Maze type (linear maze)	68	0	53
Theta frequency range ([4–10] Hz)	2568	1	2373
Velocity threshold (4,4)	2430	0	2185
Velocity threshold (6,6)	2430	0	2347
Velocity threshold (8,8)	2430	0	2410
Ripple validation (# channels: 12)	2586	1	2405
Theta detection (low level)	3856	3	3567
Theta detection (medium level)	1405	0	1314
RAT #3			
Default	1325	11	1206
Maze type (linear maze)	110	0	74
Theta frequency range ([4–10] Hz)	1615	1	1488
Velocity threshold (4,4)	1325	14	1167
Velocity threshold (6,6)	1325	6	1259
Velocity threshold (8,8)	1325	1	1283
Ripple validation (# channels: 12)	1357	14	1233
Theta detection (low level)	2402	23	2130
Theta detection (medium level)	701	3	649

The crucial parameters that were used in identifying theta ripples and behavioural state were varied to assess the implications of changing these parameters. Reported are the variations in the numbers of theta ripples, exploratory theta ripples and immobile theta ripples for parametric combination. The parameters varied were as follows: 1. **Maze type** – All the experiments were performed in the open box arena; a linear maze was used as a control for evaluating our hypothesis in a different arena. 2. **Theta frequency range** – All the analyses were done with a theta frequency range of 6–10 Hz. A lower range of 4 Hz (instead of 6 Hz) was also used as a control. 3. **Velocity thresholds** – A Default value of 5 cm s^{-1} was used as both the minimum and maximum velocity threshold for consideration as an exploratory and immobile period, respectively. Three other velocity thresholds (4, 6 and 8 cm s^{-1}) were used as controls. 4. **Ripple validation** – A default value of 10 was used as the number of channels in which ripple-like events were detected and compared to discard artifacts from the *stratum pyramidale*. Specifically, putative ripple events in the SP layer were discarded if there were events detected in at least 10 channels within 10 ms on either side of the ripple under consideration. As a control for this number, 12 channels were used for comparing and discarding artifacts from SP. 5. **Theta detection** – To quantify the strength of theta detection, a default of 1 SD above the mean signal amplitude was used as the theta detection threshold (**medium** level). As a control, 0.5 SD and 1.5 SD above the mean signal amplitude were also used as controls to signify **low** and **high** levels of detection thresholds. Default parametric combination used for analyses (listed as 'Default' below): [*Maze type*: **Open Box**; *Theta frequency range*: **[6–10] Hz**; *Velocity thresholds*: [**5 cm s^{-1}** (exp. Min. velocity), **5 cm s^{-1}** (Imm. Max. velocity); *Ripple Validation*: **10 channels**; *Theta detection*: **Medium** (1 SD above mean signal amplitude) **level**].

stringency in number of channels manifesting artifacts and the spread of ripples spanning channels proximal to the SP (e.g. ripple from Rat 1 in Fig. 1*B* spanning many channels across SO–SP–proximal SR). The 10 ms constraint on ripples detected in other channels ensured that such artifacts spreading temporally beyond the SP ripple were also discarded, even if they satisfied the spatial dispersion criteria. For all analyses reported in this study, we considered ripple events detected in the channel designated as *stratum pyramidale*.

Defining, classifying, quantifying and validating different types of ripples

Theta ripple (θ-ripple) co-occurrences were defined as events wherein a ripple detected in SP was temporally localized within a theta epoch identified from recordings from the SR or SLM layers. Such a cross-channel approach was used for the detection of theta ripples, owing to their differential expression across hippocampal *strata* (Buzsáki, 2015; Gordon et al., 2005; Mizuseki et al., 2011; Navas-Olive et al., 2022), with ripples and theta oscillations predominantly observed in SP and SR/SLM, respectively. This results in a physiological characterization of ripples based on whether they belonged to a theta epoch or not. These theta epochs that were identified independently were extended to 100 ms on either side, so that instances where ripple peak times were just outside the theta epochs while the start/end of the ripple still fell within the theta epoch were not neglected.

Cross-validating theta oscillations and ripples. We use the phrase 'classical theta' to denote epochs with strong theta frequency oscillations (6–10 Hz) in the SR-SLM band without any detected ripples in SP (Fig. 2*C*). Similarly, we used 'classical ripples' or 'non-θ ripples' to denote ripples with no theta oscillations in the SR-SLM (Fig. 2*D*). Ripples that occurred along with theta oscillations (Fig. 2*E*) were validated by quantifying several signature characteristics of ripples and comparing them with the classical non-theta ripples. The amplitude of ripples was computed as the difference between the maximal and minimal voltage values within each ripple waveform. The duration of ripples was computed as the difference between the detected start and end timestamps of a ripple. Power spectral density (PSD) analysis involved computing the Fourier transform profiles of both theta and non-theta ripple waveforms. The frequency at which the ripple PSD manifested maximal power was computed for every considered ripple waveform and averaged across all theta ripples and non-theta ripples independently. All other ripple measurements were performed on all theta and non-theta ripples. For PSD analysis, 10% of ripples from each session were chosen in a pseudorandom fashion to assess the spectral characteristics of theta *vs*. non-theta ripples.

Theta oscillations observed as part of theta ripples were validated by comparing their spectral power with theta power during classical theta epochs. Theta power was computed as the power in the theta frequency band and was computed for each detected theta epoch.

Behavioural categorization of ripples. Positional information of the rat was continuously available from time-synced video recordings of foraging behaviour (Fig. 2*A*). The instantaneous linear velocity of the rat was computed based on the Euclidean distance between successive positional co-ordinates tracked by the camera. This instantaneous velocity was used to characterize two kinds of behavioural epochs during foraging: exploratory epochs were periods with a detected running velocity >5 cm s^{-1} and immobile periods were those where the running velocity <5 cm s^{-1}. To ensure strict classification of ripples to behavioural states, immobile or exploratory periods were required to exceed a minimum duration of 1 s to be assigned to the respective epochs. Because our classification of behavioural epochs were strictly based on velocity and duration, there were ripples that were not classified into either immobile or exploratory epochs. This behavioural categorization (exploratory *vs*. immobile behavioural epochs), in addition to the electrophysiological characterization (theta *vs*. non-theta ripples) resulted in four different kinds of ripples that are based on electrophysiology and behaviour: exploratory theta (exp. θ); exploratory non-theta (exp. non-θ); immobile theta (imm. θ); and immobile non-theta (imm. non-θ).

Fraction and frequency of ripples. The proportions of different kinds of ripples in a session were computed as the ratio of the number of ripples belonging to a specific category to the total number of ripples in that session. For example, the fraction of exploratory θ ripples was computed as the ratio between number of exploratory θ ripples and the total number of ripples. The frequency of ripple occurrence was computed as the ratio of the number of ripples in a certain category to the total duration spent by the rat in that category. For example, the frequency of occurrence of exploratory θ ripples was computed as the number of exploratory θ ripples divided by the total duration of exploratory theta epochs. These measurements were computed for each session and plotted to emphasize the heterogeneities across sessions.

Analysis of theta power during ripple periods. To quantify the strength of theta oscillations during ripples, power in the theta frequency band was computed during a 50 ms period on either side of the peak of the detected ripple (total 100 ms). We computed power in the theta frequency band of the SR/SLM channel signals around every detected SP ripple. This theta power was computed as the magnitude of the wavelet spectrum in the 6–10 Hz band that was averaged for the time period. This process was executed for every ripple in every session.

Phase analyses. To quantify the temporal relationship between theta oscillations and ripples during co-occurrence events, we first computed the troughs of the theta signal as the local minima of the oscillatory waveform. Then, we computed the phase of the peak of

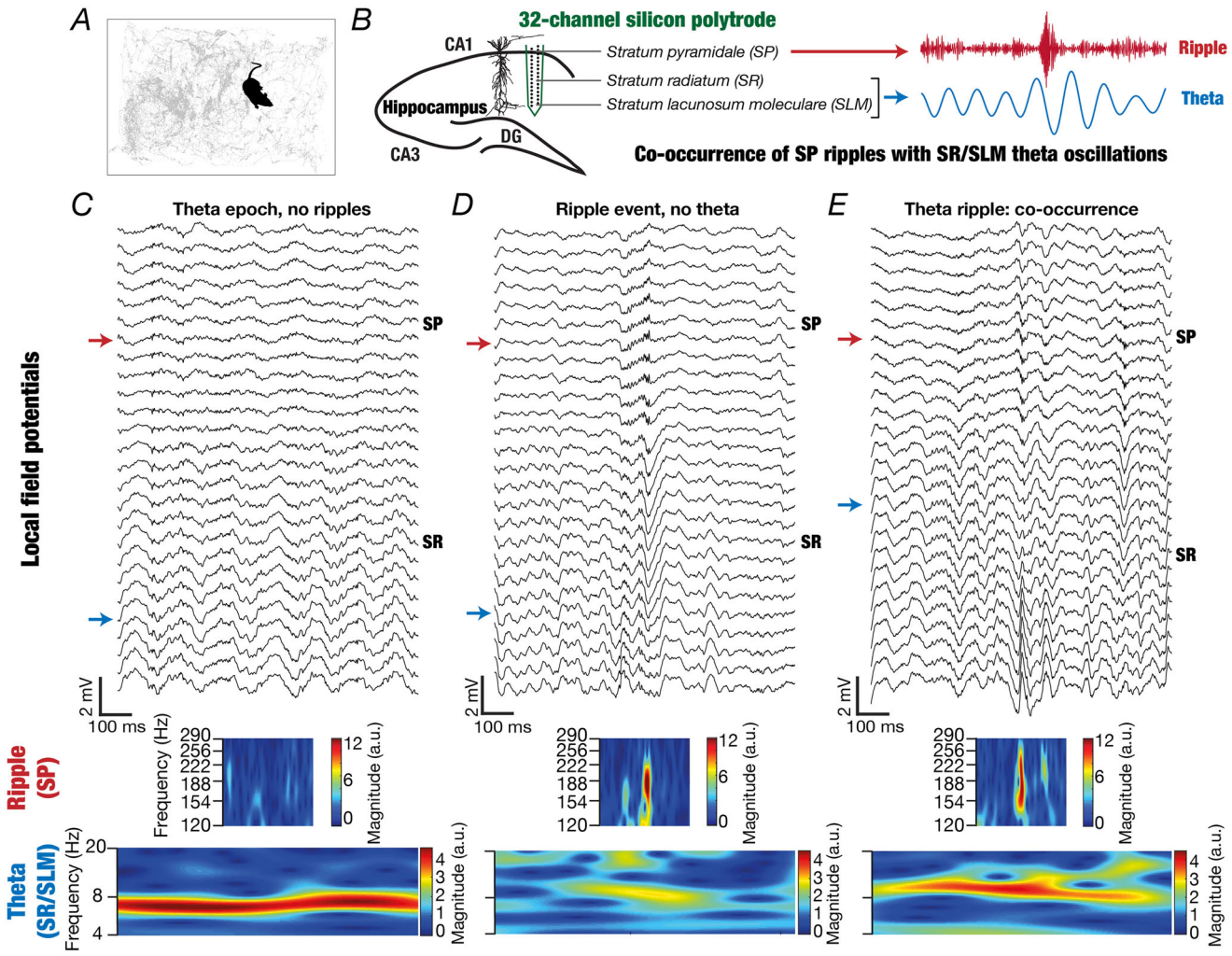

Figure 2. Co-occurrence of theta-frequency oscillations and ripples in a foraging rat
A, trajectory (grey lines) of a rat in the arena (59 cm × 49 cm) from an example recording session. *B*, left: schematic of the hippocampus proper with a single dorsal CA1 pyramidal neuron shown for illustration. Adjacent to the neuron is the sketch of a 32 channel silicon polytrode. The black circles within the electrode are representative of electrode locations relative to the neuron, spanning across the *stratum lacunosum-moleculare* (SLM) to *stratum pyramidale* (SP) stretch. Right: ripple- (top) and theta-frequency (bottom) filtered traces of extracellular voltage recordings simultaneously acquired from the SP and SR/SLM, respectively. In these example recordings, theta oscillations in the SR/SLM electrode co-occur with a ripple event in SP electrode. Such ripples in the SP co-occurring with theta-oscillations in the SR/SLM electrode are defined as theta ripples. *C–E*, top: laminar profiles of simultaneous LFP recordings during a classical theta epoch specifically showing that the theta amplitude is higher in SR/SLM electrodes compared to SP electrodes (*C*); a classical sharp wave ripple (SPW-R) complex with sharp waves predominantly visible in the SP-SR electrodes (*D*); and a co-occurrence event where a ripple in the SP electrodes is embedded within theta-oscillations that are observed prominently in the SR electrodes (*E*). Red and blue coloured arrows refer to the identified SP and SR/SLM *strata*, respectively, used for time-frequency analysis below. (*C–E*, middle) Wavelet spectrograms of the SP LFP trace shown for the ripple-frequency range (120–250 Hz) indicating the clear prevalence of ripples in (*D*) and (*E*). (*C–E*, bottom) Wavelet spectrograms of the SR/SLM LFP trace in the theta-frequency range (6–10 Hz) demonstrating strong theta oscillations in (*C*) and (*E*). Note that the spectrograms were obtained from SP or the SR/SLM LFP trace without any additional filtering in the ripple or the theta frequency ranges. More examples of theta ripples are provided in Figs 3 and 4 and another example of a non-theta ripple is given in Fig. 4. [Colour figure can be viewed at wileyonlinelibrary.com]

the ripple detected in the SP with respect to the theta oscillation detected in SR/SLM using:

$$\phi\,(t_R) \;=\; \left(\frac{t_R - t_0}{t_1 - t_0}\right) \times 360$$

where t_R corresponds to ripple peak time, and t_0 and t_1 correspond to theta trough time points that precede and succeed t_R, respectively. Specifically, the difference between the ripple peak time and the time of the trough of the theta wave that preceded the ripple peak was normalized by the difference between the times of troughs of the theta wave that encompassed this ripple. This fraction was then multiplied by 360 to compute the phase of the ripple peak time relative to the extracellular theta wave in degrees. We employed this procedure to compute the phases of ripple peak times detected in SP with respect to the theta oscillation from SR/SLM for all theta ripples.

***Strata*-dependence of co-occurrences.** We computed the number of co-occurrences of ripples and theta oscillations as a function of the identity of channel that was used to identify theta epochs. Specifically, whereas ripple frequency information was consistently obtained from the identified SP channel, theta epochs were identified independently from all recording channels. The number of theta ripples within each session was computed by calculating the number of ripples that were within theta epochs identified from different recording channels.

Long *vs.* short ripples. Ripples with a duration >80 ms were referred to as long ripples, whereas those <80 ms were considered as short ripples. The fractions of long and short ripples within theta epochs and the fractions of theta and non-theta ripples that were long were computed for each session for all rats.

Histological verification

After the completion of all recordings, we performed histological analysis of the hippocampus to verify the precise location of surgical implants. We applied a potential difference of 9 V between all 32 electrode sites and a ground site (pinna of the ear) for ∼9 s per electrode site of the implant, under deep anaesthesia (ketamine-xylazine). After waiting for a day for gliosis to set in, we anaesthetized the animal with ketamine-xylazine and then performed transcardial perfusion of paraformaldehyde (PFA) under deep anaesthesia. This ensured high contrast staining of the lesioned electrode implant site. The animal was decapitated after the completion of perfusion and the brain was carefully extracted. The extracted brain was preserved in PFA for 1–2 days following which we prepared coronal slices of 60–150 μm thickness of the implanted hippocampus using a vibratome (Leica, Wetzlar, Germany). The slices were allowed to dry overnight following which we performed cresyl violet staining. We then mounted slides with DPX mounting medium, left them to dry overnight, and imaged the lesioned implant site of the hippocampus on the following day.

Details of data and statistical analyses

All data analyses were performed with custom-written scripts that recruited the toolbox (https://fmatoolbox.sourceforge.net) in MATLAB (MathWorks Inc., Natick, MA, USA). All statistical analyses were performed using the R computing and statistical software (R Core Team, 2013). To avoid false interpretations and to emphasize the heterogeneities across ripples, sessions and rats, the entire range of measurements are reported in figures rather than providing only the summary statistics (Marder & Taylor, 2011; Rathour & Narayanan, 2019). Because data distributions were skewed across all measurements that were considered, we avoided the use of parametric statistical tests. Instead, we used non-parametric statistical tests across all figures where statistical analyses were performed. Specifically, when there were multiple groups, we first performed a Kruskal–Wallis test across all groups. We then used a Wilcoxon rank sum test or a Wilcoxon signed rank test for individual pairs in the group (or the two groups when there were only two groups to compare), depending on whether the test was unpaired or paired, respectively. The actual P values for the Kruskal–Wallis and the Wilcoxon tests are provided where appropriate. In addition, in a separately uploaded (Statistical Summary Document, Supporting Information, Doc. S1) Excel file (Microsoft Corp., Redmond, WA, USA), there are different sheets of data for each figure/panel where statistical analyses are elaborated in detail. The sheet corresponding to each figure contains the actual data points that were employed in constructing the graphs, the statistical tests that were performed and the exact P values for each statistical test that was performed. Separate sheets are also provided for each rat containing data about each detected ripple with information on the day, the arena and the session those theta/non-theta ripples were detected.

Results

Cross-*strata* co-occurrence of theta frequency oscillations with ripples

Theta-frequency oscillations and ripples are predominantly found in different hippocampal *strata*. Theta frequency oscillations are rich within the *stratum lacunosum-moleculare* (SLM) and *stratum radiatum* (SR), whereas ripples are prominent in the *stratum pyramidale*

(SP) (Gordon et al., 2005). To account for such differential prevalence of different bands of extracellular signals, we simultaneously recorded extracellular field potentials from different hippocampal *strata* of awake behaving rodents that were involved in a foraging task within an open arena (Fig. 1 and Fig. 2A). Simultaneous acquisition of signals spanning different *strata* using 32 channel silicon polytrodes allowed us to identify each *stratum* using respective characteristic electrophysiological signatures, and to assess the co-occurrence of ripples in the SP with theta-frequency oscillations in the SR/SLM (Fig. 2*B*).

We identified all ripples (total ripples: Rat 1: 5293; Rat 2: 8320; Rat 3: 8006) from the SP channel and asked if any of these identified ripples were embedded within epochs of theta oscillations deduced from the SR/SLM LFP. Strikingly, we found several instances of ripple events delineated from the SP signal to be embedded within epochs of theta-frequency oscillations recorded within SR/SLM (Fig. 2*B*). We defined such ripples that occurred within identified theta epochs as theta (θ) ripples (examples: Fig. 2*E*, Fig. 3 and Fig. 4*A*–*D*) and distinguished them from classical non-theta (non-θ) ripples that occurred outside of theta epochs (examples: Fig. 2*D* and Fig. 4*E*–*H*). The overall proportion of θ ripples across all rats, spanning all behavioural sessions in the open arena, was around 18% (% θ ripples: Rat 1: 444/5293 = 8.4%; Rat 2: 2430/8320 = 29.2%; Rat 3: 1325/8006 = 16.6%). Wavelet scalograms of recordings involving different cross-*strata* combinations – theta oscillations without ripples (Fig. 2*C*), non-theta ripples (Fig. 2*D*) and theta ripples (Fig. 2*E*) – quantitatively

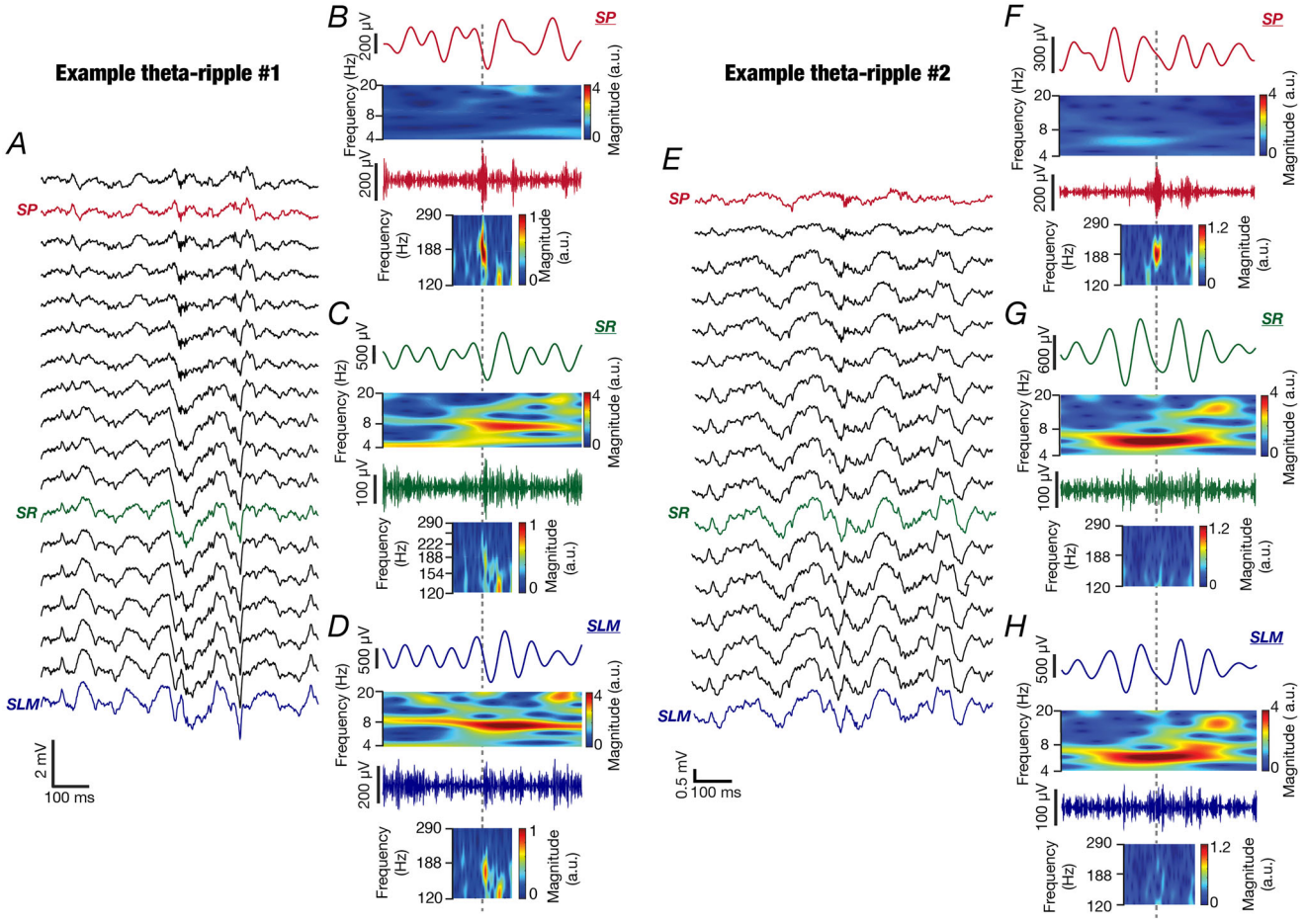

Figure 3. Example theta ripples
A–*D*, theta ripple co-occurrence example 1 from Rat 1: *strata*-wise theta- and ripple-frequency spectrograms. *A*, laminar profile of local field potentials recorded during a theta ripple co-occurrence event with red, green and blue traces indicating SP, SR and SLM, respectively. *B*–*D*, theta- (top) and ripple- (bottom) frequency filtered traces and wavelet scalograms for the three identified *strata*. It may be noted that the theta oscillation was strongest in the SLM, whereas the ripple was prominently observed in the SP. The colour scale for both theta- and ripple-frequency wavelet scalograms is matched across panels. All scalograms were on unfiltered LFP traces. *E*–*H*, theta ripple co-occurrence example 2 from Rat 3: *strata*-wise theta- and ripple-frequency spectrograms. All details same as in (*A*) to (*D*). [Colour figure can be viewed at wileyonlinelibrary.com]

confirmed the presence (Fig. 2*C*, Fig. 2*E*, Fig. 3 and Fig. 4*A*–*D*) or absence (Fig. 2*D* and Fig. 4*E*–*H*) of strong theta oscillations in the SR/SLM channel, concurrent with ripple presence (Fig. 2*D*–*E* and Figs 3–4) or absence (Fig. 2*C*) in the SP channel.

A majority of theta ripples occurred during immobile periods of the foraging rat

We divided the behavioural state of the foraging animal into exploratory and immobile periods based on cut-offs on instantaneous velocity and epoch duration. We classified ripples into two categories based on whether they were observed during the exploratory (exp. ripple) or the immobile (imm. ripple) behavioural phases. Together with the electrophysiological categorization of ripples into theta and non-theta ripples, the behavioural state of the animal provided four distinct categories of ripples: exploratory theta (exp. θ), exploratory non-theta (exp. non-θ), immobile theta (imm. θ) and immobile non-theta (imm. non-θ). We examined the fraction and frequency of occurrence of the four different kinds of ripples based on electrophysiological and behavioural co-occurrences (Fig. 5). The immobile non-θ ripples constituted a major proportion of all ripples (~80% across all rats), whereas most of the remaining 20% of ripples were immobile

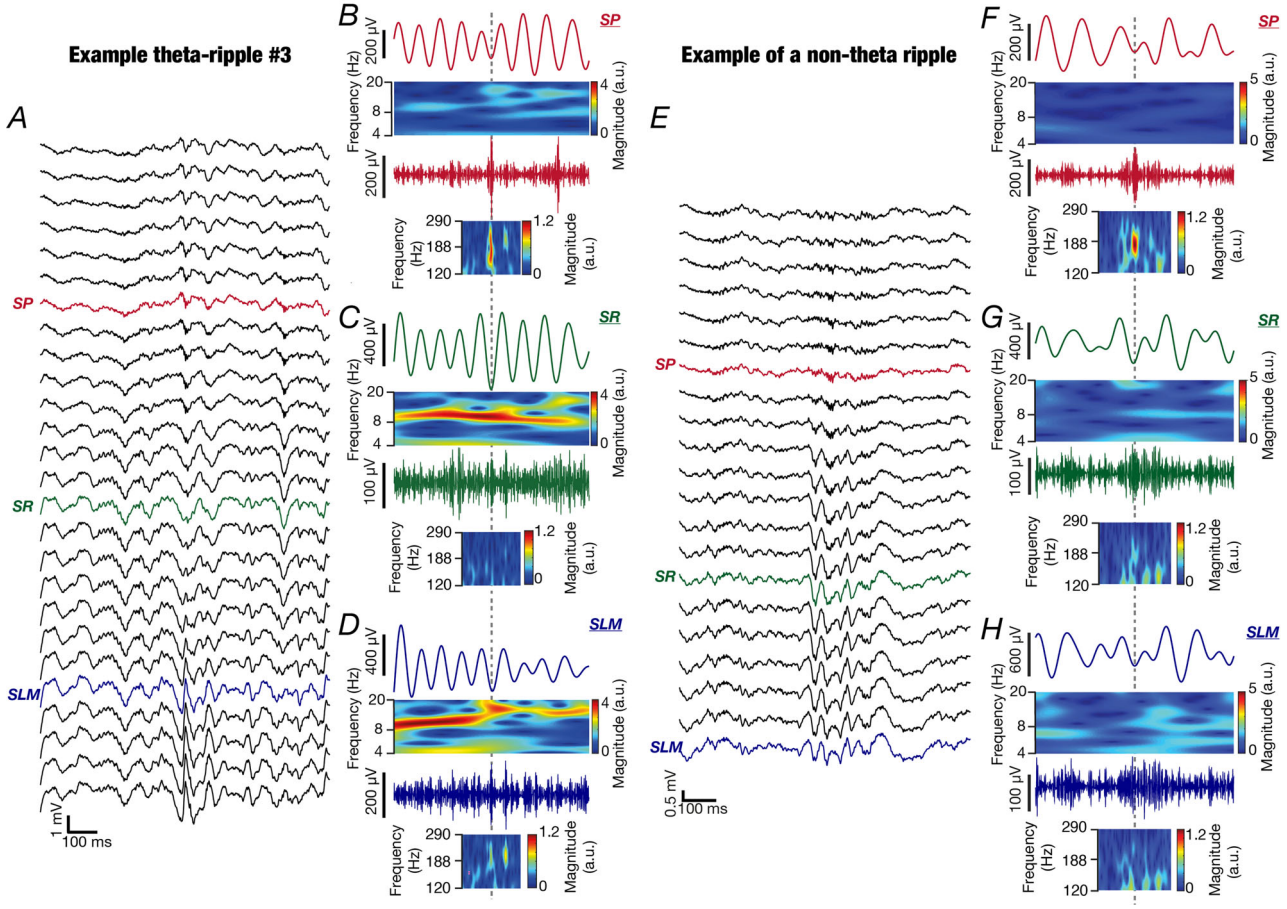

Figure 4. Example theta and non-theta ripples
A–D, theta ripple co-occurrence example 3 from Rat 1: *strata*-wise theta- and ripple-frequency spectrograms. *A*, laminar profile of local field potentials recorded during a theta ripple co-occurrence event with red, green, and blue traces indicating SP, SR and SLM, respectively. *B–D*, theta- (top) and ripple- (bottom) frequency filtered traces and wavelet scalograms for the three identified *strata*. It may be noted that the theta oscillation was strongest in the SLM, whereas the ripple was prominently observed in the SP. The colour scale for both theta- and ripple-frequency wavelet scalograms are matched across panels. All scalograms were on unfiltered LFP traces. *E–H*, non-theta ripple example from Rat 1: *strata*-wise theta- and ripple-frequency spectrograms. *E*, laminar profile of local field potentials recorded during a sharp wave ripple (SPW-R) event with red, green and blue traces indicating SP, SR and SLM, respectively. *F–H*, theta- (top) and ripple- (bottom) frequency filtered traces and wavelet scalograms for the three identified *strata*. It may be noted that the theta oscillations were not observed in any of the channels. The ripple was prominently observed in the SP. The colour scale for both theta- and ripple-frequency wavelet scalograms is matched across panels. All scalograms were on unfiltered LFP traces. [Colour figure can be viewed at wileyonlinelibrary.com]

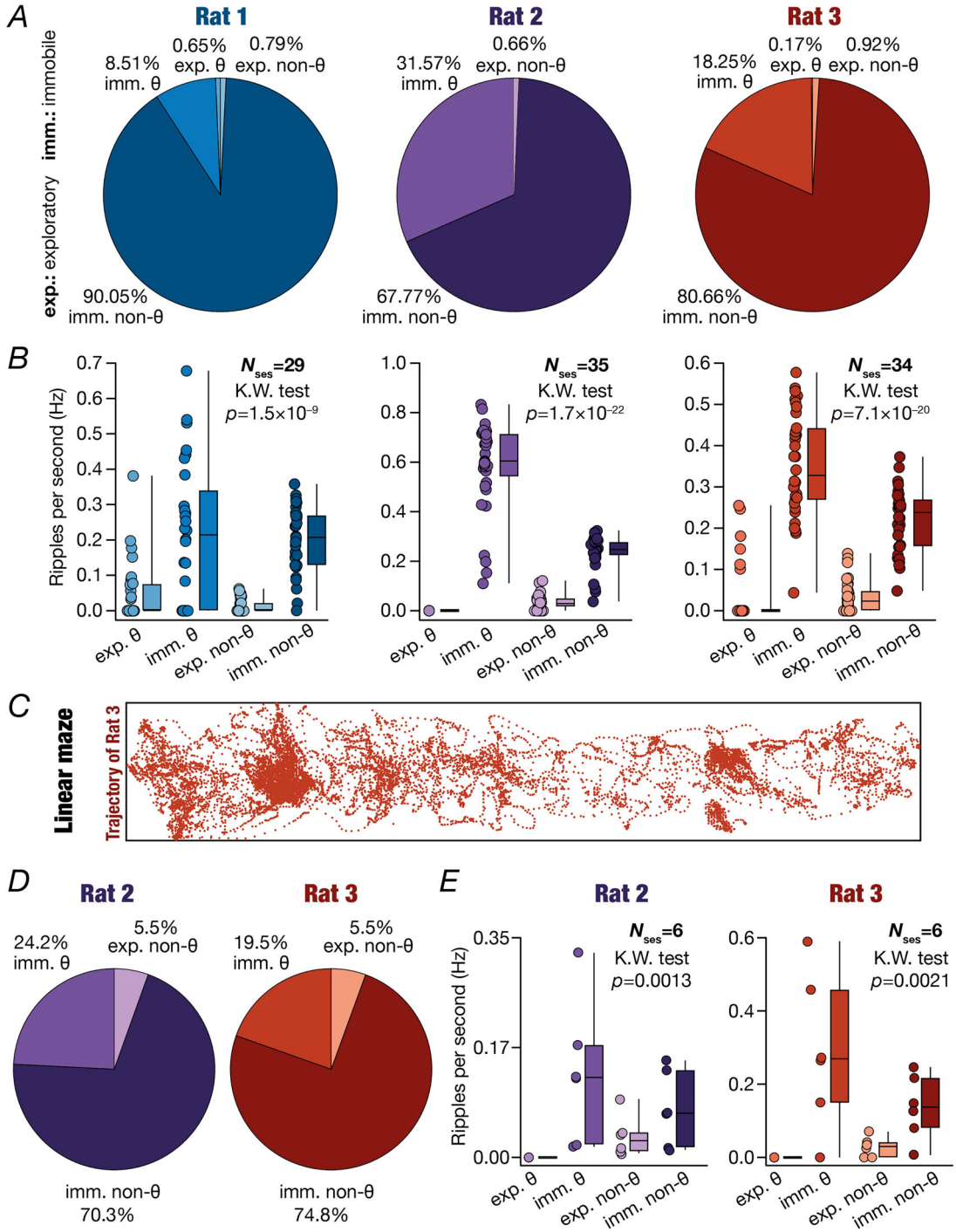

Figure 5. Fraction and frequency of different kinds of ripples in an open arena and a linear maze
A and *B*, represent data from an open arena and (*C*–*E*) are from a linear maze. *A*, pie charts representing proportions of the four kinds of ripples – exploratory theta (exp. θ); immobile theta (imm. θ); exploratory non-theta (exp. non-θ); and immobile non-theta (imm. non-θ) – for the three rats spanning all recording sessions. *B*, frequency of occurrence of ripples for the four ripple kinds, provided for all recorded sessions. In all plots, a box plot showing respective median values and the interquartile ranges are also depicted. The *P* values computed with the Kruskal–Wallis (K.W.) test are provided for each rat. The group-wise Wilcox rank sum test *P* values: Rat 1: exp. θ *vs.* imm. θ: 0.0012, imm. θ *vs.* exp. non-θ: 2.1×10^{-4}, exp. non-θ *vs.* imm. non-θ: 7.1×10^{-20}, exp. θ *vs.* imm. non-θ: 6.1×10^{-7}, exp. θ *vs.* exp. non-θ: 0.3775, imm. θ *vs.* imm. non-θ: 0.85; Rat 2: exp. θ *vs.* imm. θ: 1.7×10^{-9}, imm. θ *vs.* exp. non-θ: 7.6×10^{-13}, exp. non-θ *vs.* imm. non-θ: 3.2×10^{-12}, exp. θ *vs.* imm. non-θ: 1.7×10^{-9}, exp. θ *vs.* exp. non-θ: 5.9×10^{-7}, imm. θ *vs.* imm. non-θ: 1.8×10^{-10}; Rat 3: exp. θ *vs.* imm. θ:

2.0×10^{-10}, imm. θ *vs*. exp. non-θ: 3.1×10^{-12}, exp. non-θ *vs*. imm. non-θ: 8.1×10^{-12}, exp. θ *vs*. imm. non-θ: 1.2×10^{-8}, exp. θ *vs*. exp. non-θ: 0.032, imm. θ *vs*. imm. non-θ: 5.1×10^{-6}. *C*, linear maze trajectory of a rat in an example recording session. *D*, pie charts representing proportions of the four kinds of ripples – exploratory theta (exp. θ); immobile theta (imm. θ); exploratory non-theta (exp. non-θ); and immobile non-theta (imm. non-θ) – for the two rats spanning all recording sessions. *E*, frequency of occurrence of ripples for the four ripple kinds, provided for all recorded sessions. In all plots, a box plot showing respective median values and the interquartile ranges are also depicted The *P* values computed with the Kruskal–Wallis (K.W.) test are provided for each rat. The group-wise Wilcox rank sum test *P* values are provided in the attached Statistical Summary Document, Supporting Information, Doc. S1. [Colour figure can be viewed at wileyonlinelibrary.com]

θ ripples. Exploratory ripples during the foraging task were very few, irrespective of whether SP ripples occurred with or without co-occurring SR/SLM theta oscillations (Fig. 5*A*). Notably, across sessions, the frequency of immobile theta ripples was significantly higher than immobile non-θ ripples in Rats 2–3, whereas the two quantities were comparable in Rat 1 (Fig. 5*B*). These observations imply that the probability of observing more immobile θ ripples adjacent to each other is higher than that for the other three kinds of ripples. In two of the rats (Rats 2–3), we repeated our experiments and analyses in another arena, a linear maze (Fig. 5*C*–*E*). Our conclusions about the proportions of different ripple subtypes (Fig. 5*D*) and frequencies of their occurrence were consistent across the open arena (Fig. 5*A* and *B*) and the linear maze (Fig. 5*C*–*E*). It is essential to note that there was pronounced animal-to-animal (Rat 1: 8.4%; Rat 2: 29.2%; Rat 3: 16.6%) and session-to-session (Fig. 5*B* and Fig. 5*E*) variability in the manifestation of theta ripples. However, we found that the number and proportion of theta ripples detected were comparable across days and across different arenas (see Statistical Summary Document, Supporting Information, Doc. S1).

Theta and non-theta ripples had comparable characteristics

Are theta ripples distinct from non-theta ripples with reference to the several signature characteristics of ripples? To address this, we computed multiple signature measurements associated with all the detected ripples (maximum frequency, amplitude, duration, power, velocity, SR/SLM theta power during the ripple) and compared them for theta *vs*. non-theta ripples (Figs 6 and 7). We found all ripple measurements (maximum frequency, amplitude, duration, power) and their distributions to be similar between the theta and the non-theta groups, across all three rats (Fig. 6*A*–*C* and Fig. 7). Because most ripples occurred during immobile periods (velocity <5 cm s^{-1} for at least 1 s), the velocity of the animal during ripple occurrences were also comparable for theta *vs*. non-theta ripples (Fig. 7). These analyses demonstrated that theta-ripples were not intrinsically distinct from traditional non-theta ripples.

Because theta power distinguished theta and non-theta ripples, we found the theta power (see histograms of 'during-ripple theta power' for each rat in Figs 7*A*–*D*, comparing theta ripples and non-theta ripples) during the occurrence of the ripple to be significantly higher for theta ripples compared to that for non-theta ripples (Fig. 7). Importantly, theta power in the SR/SLM channel during theta ripples (50 ms on either side around the peak of the ripple) was comparable (Fig. 6*D* and Fig. 7*D*) with theta power observed during theta epochs (power computed across the entire epoch). Our analyses pipeline requiring a theta-ripple to be nested within a stream of theta oscillations (theta epoch) and quantitative demonstration of significantly lower theta power in the vicinity of non-theta ripples (compared to their theta ripple counterparts) clearly demarcate theta ripples from non-theta ripples. In addition, theta and non-theta ripple measurements did not show strong pairwise relationships, except for the expected strong relationship between theta power and theta amplitude (Fig. 7*A*–*C*). Intriguingly, the average theta frequency in immediate vicinity of theta ripples, although within the theta-frequency range, was significantly higher compared to the average theta frequency in theta epochs (Fig. 8). However, this increase in average theta frequency was limited to the 400 ms duration (200 ms on either side of theta ripples) and returned to lower values when the average was computed over 1000 ms or 2000 ms periods (500 ms or 1000 ms on either side of theta ripples, respectively) (Fig. 8). This small yet significant increase in average theta frequency could be consequent to interactions of SR/SLM theta with sharp waves that co-occur with ripples.

Although the overall durations of theta and non-theta ripples were comparable (Fig. 6*C*), we considered whether there were differential expression profiles of long *vs*. short ripples (cut-off: 80 ms) within theta epochs (Fig. 9). We found session-to-session and animal-to-animal variability in the proportions of short/long ripples within theta epochs (Fig. 9*A* and *B*), although the overall proportions of short/long ripples followed the percentage of theta ripples among all identified ripples (Fig. 5*A*). The percentage of theta or non-theta ripples that were long also manifested variability across sessions and animals but were comparable in their ranges (Fig. 9*C* and *D*). Together, these analyses (Figs 6–9) demonstrated that theta ripples showed similar characteristics as their non-theta counterparts and that the theta-frequency power during theta ripples and during theta epochs were comparable.

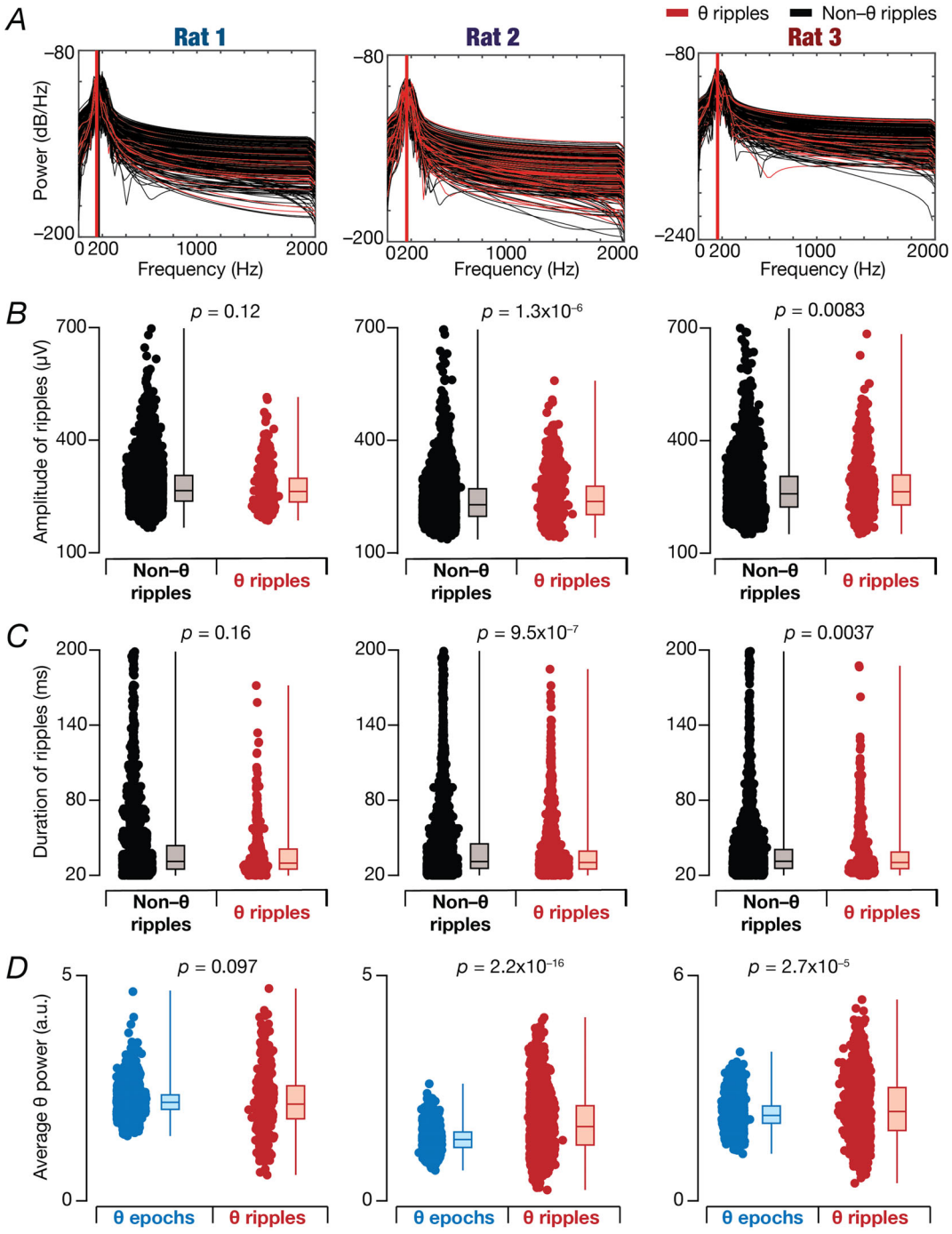

Figure 6. Comparable characteristics of theta and non-theta ripples
A–C, comparative assessment of the defining characteristics of non-theta and theta ripples, demonstrating the validity of theta ripples. *A*, power-spectral density (PSD) of non-theta (black) and theta (red) ripple traces, showing comparable spectral properties of theta and non-theta ripples. Each PSD trace corresponds to an individual ripple. From every session, a random set of 10% of ripples were chosen for this illustration. The vertical lines indicate the average frequency of maximal power for non-theta (black) and theta (red) ripples. *B–C*, comparable amplitudes (*B*) and durations (*C*) of non-theta (black) and theta (red) ripples. Each point refers to individual ripples obtained across all sessions in each of the three rats. *D*, comparable magnitudes of theta power during classical theta epochs (blue) and during theta-ripple events (red, 50 ms on either side of the peak of the ripple; total 100 ms period in ripple vicinity) shows the validity of theta oscillations observed during theta ripple events. Each point refers to the individual theta epochs or individual theta ripples across all sessions. *P* values in (*B*) to (*D*) correspond to Wilcox rank sum test. In all plots in (*B*) to (*D*), a box plot showing respective median values and the interquartile ranges are also depicted. [Colour figure can be viewed at wileyonlinelibrary.com]

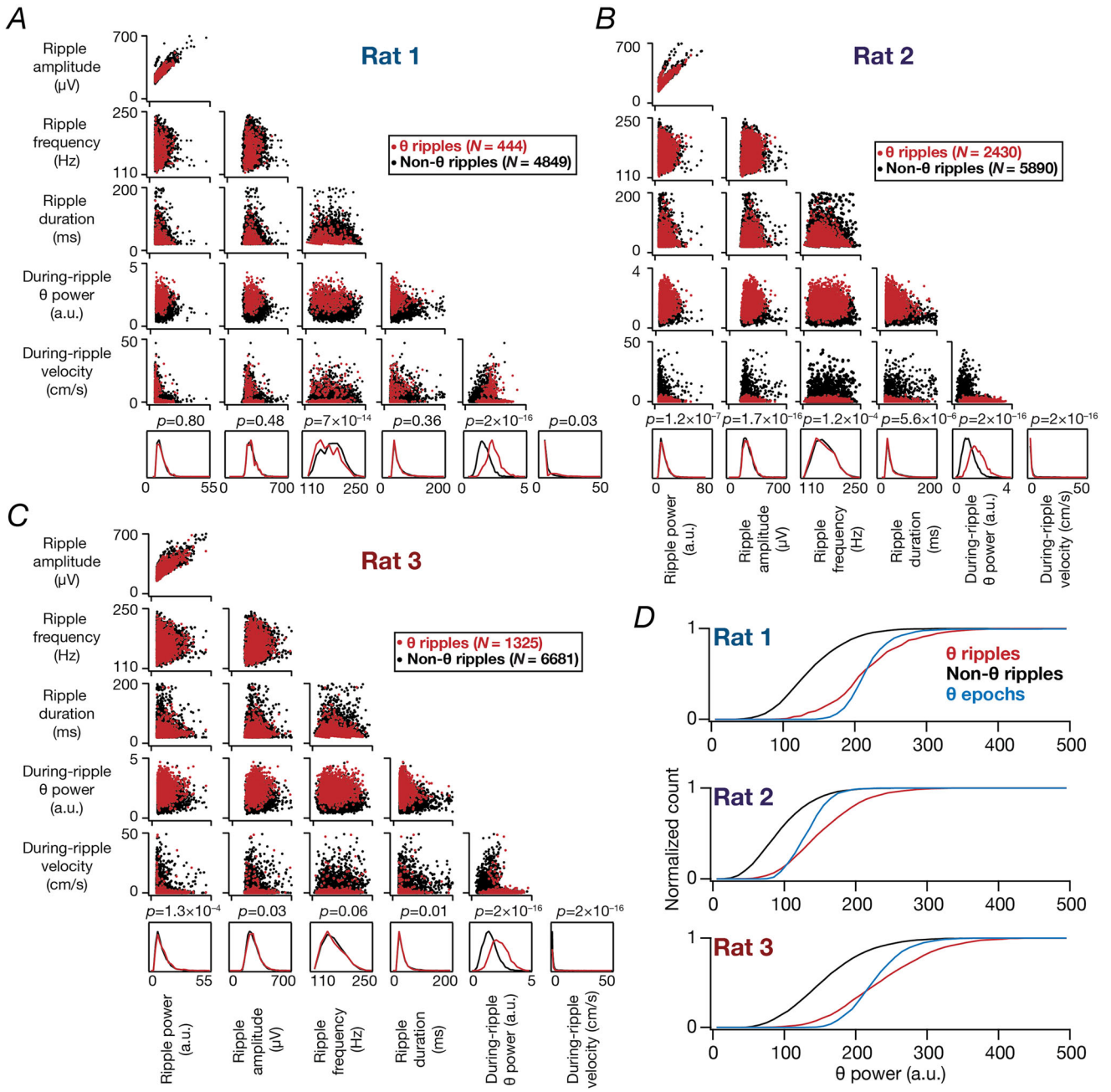

Figure 7. Pairwise relationships between characteristics of theta and non-theta ripples
A, comparing pairwise relationships between characteristics of theta and non-theta ripples for Rat 1. Scatter plots of pairwise dependencies between six characteristic measurements pertaining to ripples: power, amplitude, frequency, duration, theta power during ripple and velocity of the rat during ripple. The theta power during ripple was taken to be the average power in the theta frequency band (6–10 Hz) in the period spanning 50 ms on either side of the peak of the ripple. Velocity during the ripple was taken to be the average velocity of the rat 150 ms on either side of the ripple peak. The last row provides the histograms of individual measurements for both theta and non-theta ripples. *P* values were computed to compare measurements for theta *vs*. non-theta ripples with the Wilcox rank sum test. The Pearson correlation coefficient values were low (<0.2) for other pairwise plots except for the top left graph showing ripple amplitude *vs*. ripple power (*R* value for theta ripples: 0.89; *R* value for non-theta ripples: 0.88). *B*, comparing pairwise relationships between characteristics of theta and non-theta ripples for Rat 2. All details are the same as (*A*). The Pearson correlation coefficient values were low (<0.2) for other pairwise plots except for the top left graph showing ripple amplitude *vs*. ripple power (*R* value for theta ripples: 0.89; *R* value for non-theta ripples: 0.87). *C*, comparing pairwise relationships between characteristics of theta and non-theta ripples for Rat 3. All details are the same as (*A*). The Pearson correlation coefficient values were low (<0.2) for other

pairwise plots except for the top left graph showing ripple amplitude *vs*. ripple power (*R* value for theta ripples: 0.82; *R* value for non-theta ripples: 0.83). *D*, histograms of during ripple (50 ms on either side of the ripple) theta power plotted for theta ripples and non-theta ripples, for each of the three rats. Also plotted is the histogram for theta power within theta epochs for comparison. [Colour figure can be viewed at wileyonlinelibrary.com]

Theta ripples preferentially occurred within the falling phase of the co-occurring theta oscillations

Do theta ripples detected in the SP occur at specific phases of the theta oscillation concomitantly detected in the SR/SLM? We examined this by computing the phase of the peak of a detected theta ripple in SP relative to the theta oscillations that were simultaneously identified in SR/SLM (example: Fig. 10*A*–*E*). Surprisingly, we found that theta ripples had a consistent phase relationship to the concomitant theta oscillations across all rats, suggesting potential interactions between these oscillatory patterns across *strata*. Specifically, theta ripples manifested a phase preference predominantly for the fourth quadrant ($3\pi/2-2\pi$ phase range) of the associated theta oscillation (Fig. 10*F*). With the trough designated as zero phase, this preference corresponds to the falling part of the theta oscillation in the SR/SLM.

Lower theta power in SP emphasizes the need for simultaneous multi-*strata* recordings in detecting theta ripples

Two important methodological differences in our experimental design and analyses were: (1) the use of simultaneous multi-*strata* recordings and (2) analysing LFPs from two different *strata* for identifying theta oscillations (SR/SLM) and ripples (SP). These experimental and analyses design paradigms were driven by the established differences in expression profiles of theta oscillations and ripples across different *strata* (Buzsaki, 2002; Gordon et al., 2005; Zutshi et al., 2022). Theta oscillations are dominant in the SLM as a result of the distal localization of entorhinal cortical inputs and progressively reduced in theta power along the SLM-SR-SP-SO axis (Buzsaki, 2002; Gordon et al., 2005; Zutshi et al., 2022). Ripples, on the other hand, are detected predominantly in the perisomatic *strata*, primarily localized to the SP (Buzsáki, 2015; Gordon et al., 2005; Navas-Olive et al., 2022).

We confirmed the differential power of theta oscillations across CA1 *strata* during exploratory and immobile periods of behaviour (Fig. 11). Specifically, our analyses demonstrated that theta power in individually identified theta epochs was higher in the SLM, with a progressive fall in power along the SLM-SR-SP-SO axis during both immobile and exploratory theta epochs. These analyses confirmed that the theta power during immobile periods (during which most theta ripples were identified) (Fig. 5) was comparable (Fig. 11) to theta power during exploratory periods (to which theta oscillations are traditionally associated with). Thus, the ability to detect theta oscillations and associated theta epochs progressively reduce if SP or SO LFP were employed for the purpose. Consequently, we hypothesized that the number of identified theta ripples should reduce if we employed SP or SO channels as the theta channel, rather than using the SR/SLM LFP that we have been using thus far.

To directly test this, we used the ripples detected from the SP channels and asked if the number of theta ripples would change if we used different channels spanning the SLM-SR-SP-SO axis for identifying theta epochs. Specifically, we picked one of the several channels that fell within this axis and used theta-filtered power in that channel to delineate theta epochs. We then asked how many of the ripples identified from the SP channel were within these theta epochs delineated from this chosen channel. We computed this count of theta ripples for each session for each of the three rats, and the whole analysis was performed for all channels along SLM-SR-SP-SO axis (Fig. 12). Strikingly, and consistent with our hypothesis, we found that number of co-occurrences between theta oscillations and ripples were significantly lower if the SP or the SO channels were used for identifying theta epochs (Fig. 12).

Discussion

The principal demonstration of the present study is the co-occurrence of theta oscillations with ripples by explicitly accounting for the differential expression profiles of theta oscillations and ripples across CA1 *strata*. Simultaneous multi-*strata* recordings from foraging rats coupled with an analysis regime that detected these oscillations in the *stratum* where their power is the highest provided the substrate for demonstrating the prevalence of theta ripples. The prevalence of theta ripples opens new avenues of investigation, specifically expanding the potential physiological roles of ripples to encoding regimes.

Experimental designs and analysis pipelines should explicitly account for cross-*strata* co-occurrence of theta oscillations and ripples

Traditionally, studies recording extracellular signals place extracellular electrodes in the SP with a focus on simultaneously capturing neuronal spiking as well as

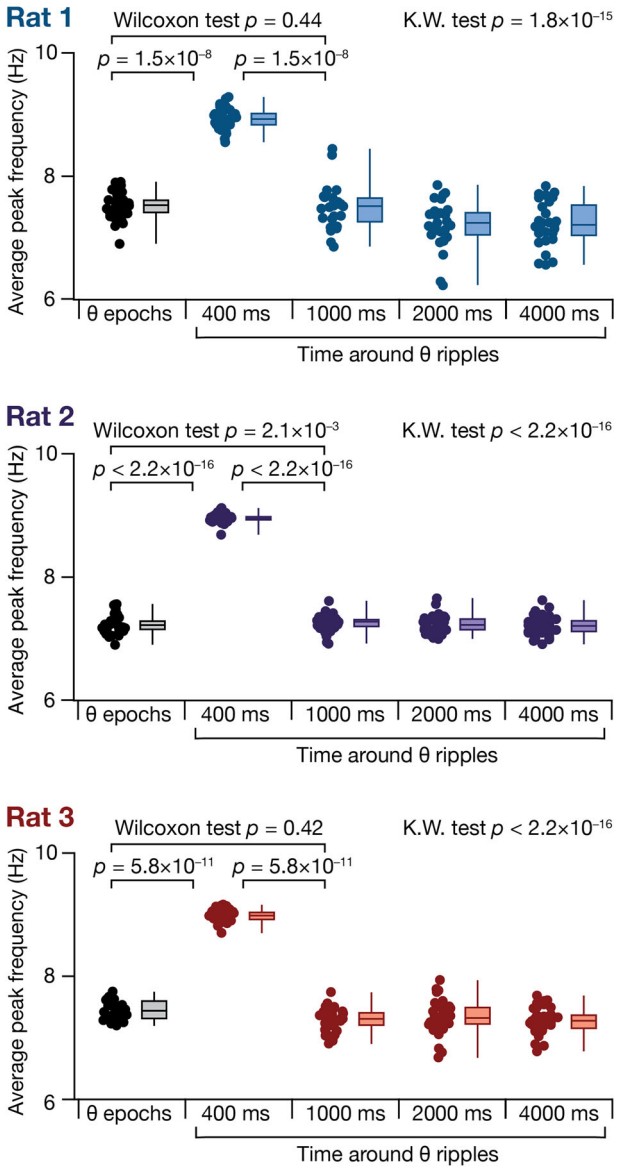

Figure 8. Increase in average theta frequency in the vicinity of theta ripples
In each rat, the average peak frequency was calculated in a session-wise manner for all theta epochs (first column) or for theta ripples (second to fourth columns) and each point corresponds to the average value computed within a given session. The average peak frequency was computed from the wavelet spectrogram of the entire LFP waveform by first noting down the frequency at which the power peaked for each timepoint within the vicinity of each theta ripple. The average of these frequency values across all theta ripples in the session were plotted as the average peak frequency for that session. In all plots, a box plot showing respective median values and the interquartile ranges are also depicted. K.W.: Kruskal–Wallis. Pairwise *P* values are provided for Wilcox signed rank test. The complete matrix of *P* values for Wilcox signed rank test across all groups is provided in the Statistical Summary Document, Supporting Information, Doc. S1. [Colour figure can be viewed at wileyonlinelibrary.com]

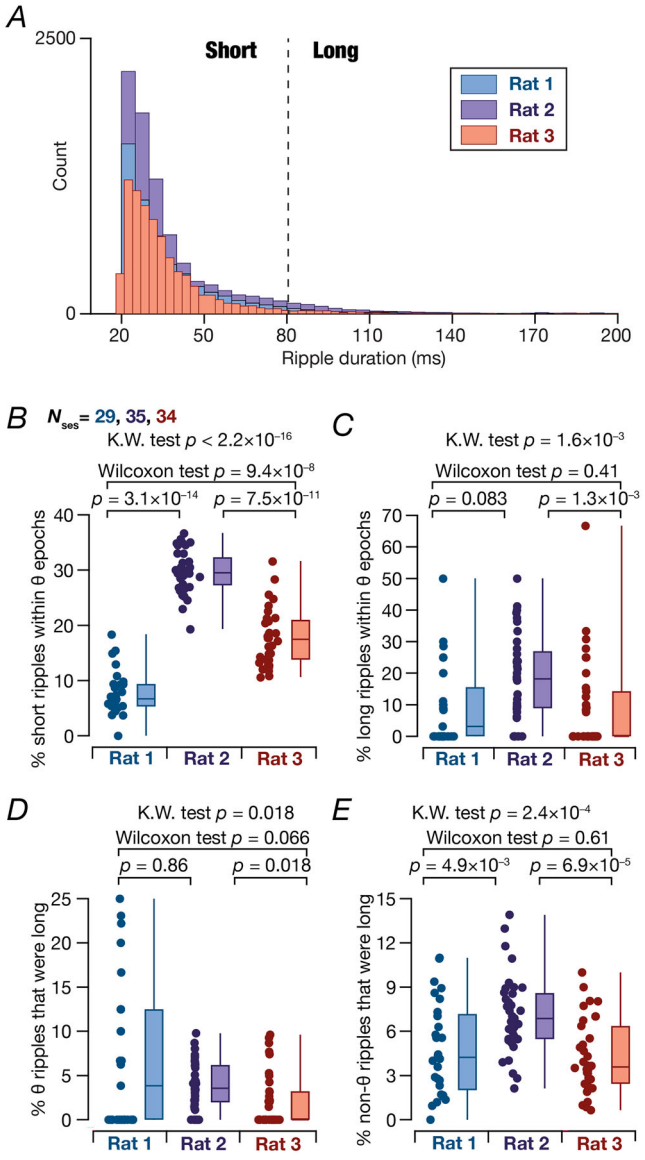

Figure 9. Distributions of ripple duration among theta and non-theta ripples
A, histograms of durations of ripples from the three rats. A cut-off of 80 ms was set to distinguish short *vs.* long ripples. *B*, percentage of short ripples that were detected within theta epochs. *C*, percentage of long ripples that were detected within theta epochs. *D*, percentage of theta ripples that were of long duration. *E*, percentage of non-theta ripples that were of long duration. In all plots, a box plot showing respective median values and the interquartile ranges are also depicted. In each rat, the percentages were calculated in a session-wise manner and each point corresponds to the respective percentage value computed within a given session. K.W.: Kruskal–Wallis. Pairwise significance is provided for Wilcox rank sum test. [Colour figure can be viewed at wileyonlinelibrary.com]

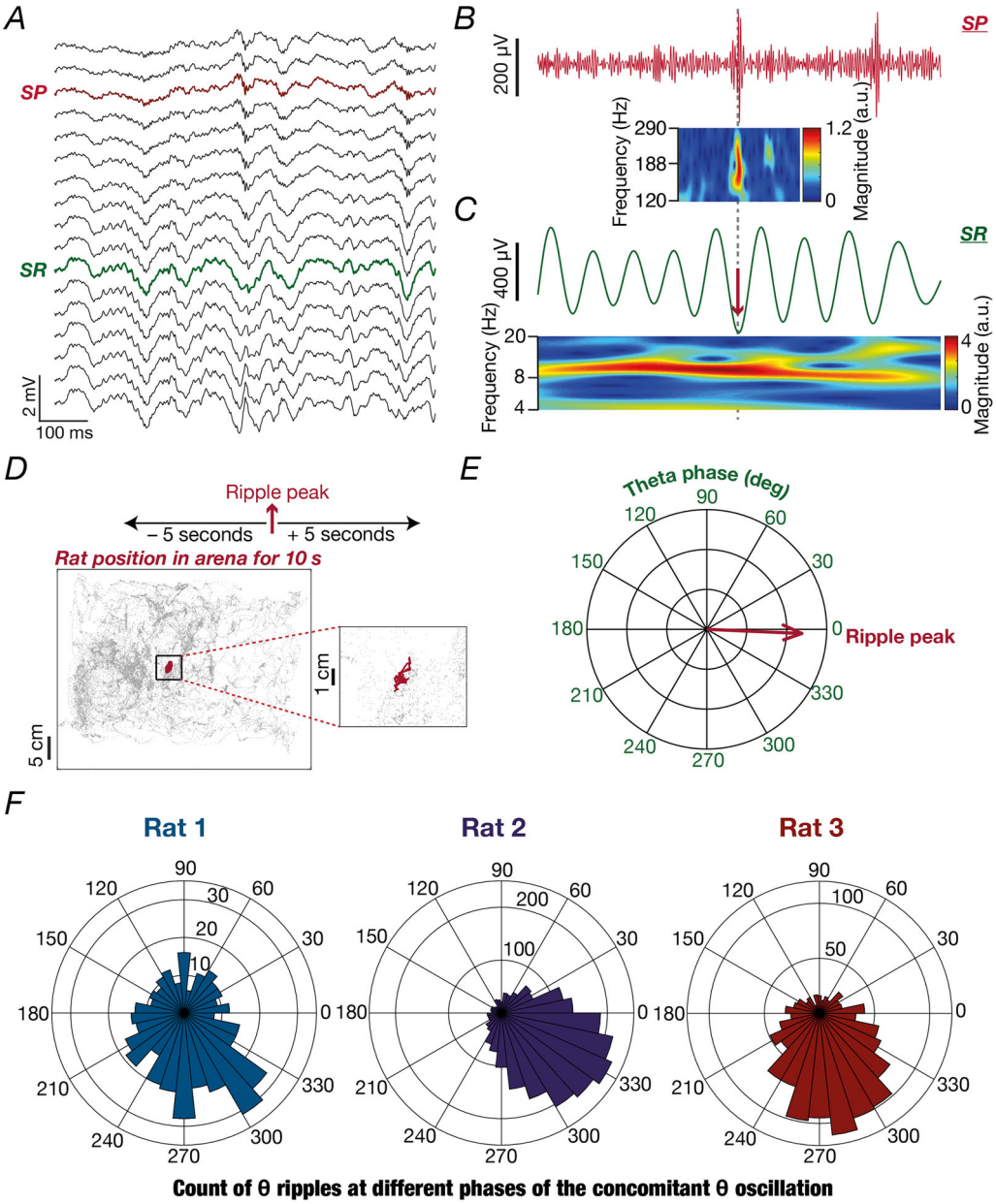

Figure 10. Phase relationship of theta ripples with co-occurring theta oscillations
A–E, an example immobile theta (imm. θ) ripple. *A*, laminar profile of local field potentials recorded during an example session from Rat 1 with the identified SP and SR marked in red and green, respectively. *B*, ripple-filtered trace and ripple-frequency wavelet scalogram of the signal recorded in SP. *C*, theta-filtered trace and theta-frequency wavelet scalogram of the signal recorded in SR. Simultaneous prevalence of ripple in SP and theta in SR may be noted both from the laminar profile (*A*) and *strata*-wise scalograms (*B–C*). *D*, trajectory of the rat 5 s before and after the ripple peak time shown in red overlaid on top of the trajectory of the rat during the entire session in grey. The zoomed inset shows the position of the rat during the 10 s period. *E*, phase of the peak of the ripple shown in (*B*) detected in SP with respect to the trough of the simultaneously recorded theta oscillation shown in (*C*) detected in SR. *F*, polar histogram showing the distribution of phases of the peak of the ripple (SP channel) with respect to the theta oscillations (SR/SLM channel) during theta-ripple events for all rats. It may be noted that phases of theta ripples show a preference for the fourth quadrant of the theta oscillation. Zero degrees represented the trough of the theta oscillation. [Colour figure can be viewed at wileyonlinelibrary.com]

extracellular field potentials from the cell bodies that are predominantly located in the SP. The focus on the SP also extends to studies that have concomitantly recorded intra- and extra-cellular potentials. However, as later studies have elucidated, it is important to measure extracellular signals from *strata* other than the SP that would reflect dendritic potentials, in addition to deriving individual units by proximal placement of electrodes to the cell bodies (Buzsaki, 2015; Gordon et al., 2005; Kamondi, Acsady, Wang et al., 1998; Sinha & Narayanan, 2022). The fundamental question posed in the present study required us to acquire across-*strata* extracellular

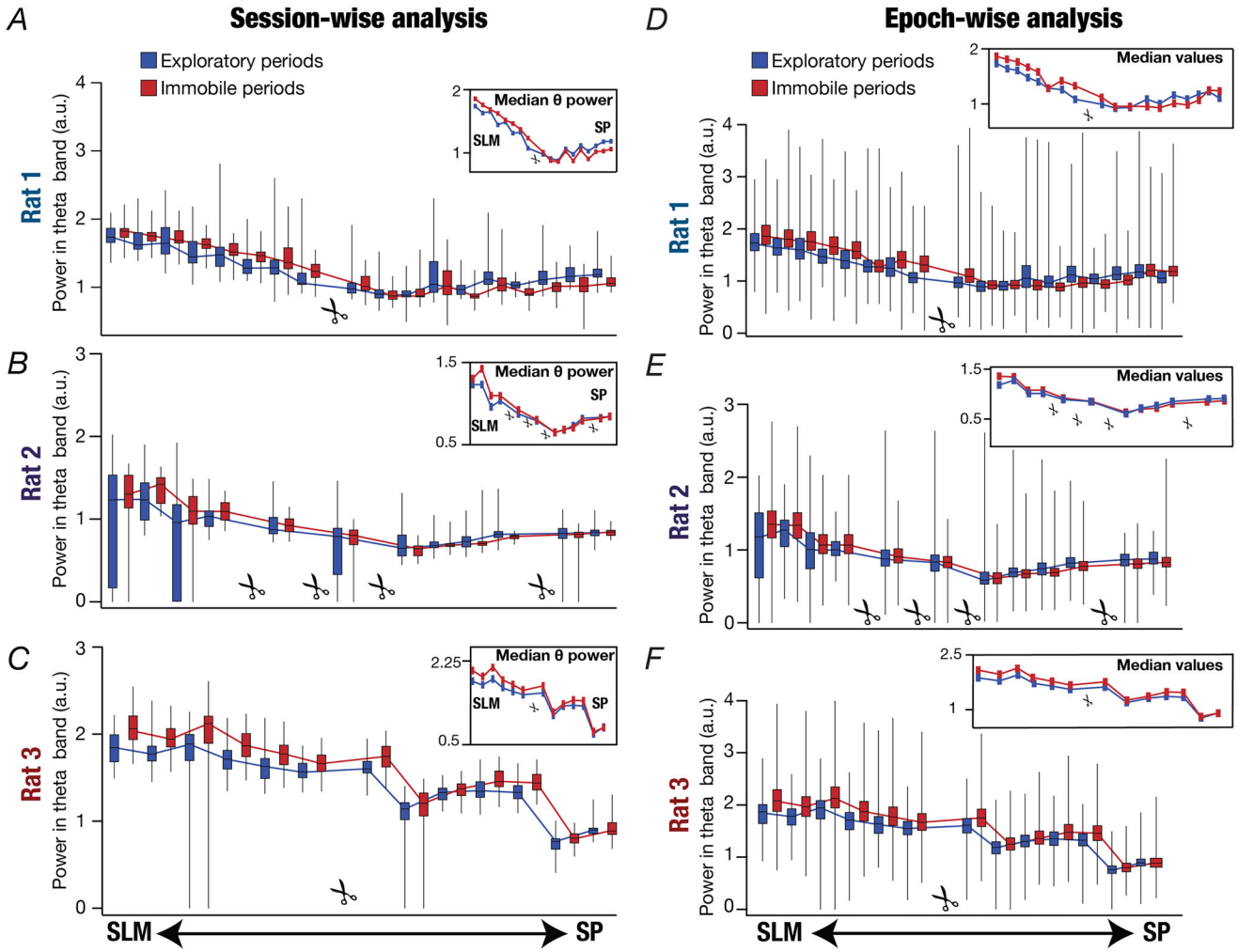

Figure 11. Theta power was highest in SLM with a progressive power reduction through SR to SP during immobile and exploratory periods
A–C, theta power during immobile and exploratory periods obtained from recording channels spanning different *strata* (SLM to SP) for the three rats across all recording sessions. The insets show the *stratum*-dependent median power values computed from the respective points shown in the main plots. A symbol showing a pair of scissors indicates that the specific recording channel was noisy for a majority (≥90%) of the recorded sessions and was discarded from analyses. *A–C*, representing different rats (Rats 1–3). Wilcox rank sum test *P* values for theta power computed from the identified SLM *vs*. SP channel: Rat 1: SLM *vs*. SP: 3.18×10^{-12} (exp.), 7.4×10^{-12} (imm.); Rat 2: SLM *vs*. SP: 4.91×10^{-7} (exp.), 2.2×10^{-16} (imm.); Rat 3: SLM *vs*. SP: 2.2×10^{-16} (exp.), 2.2×10^{-16} (imm.). *D–F*, theta power during immobile and exploratory periods obtained from all detected theta epochs from recording channels spanning different *strata* (SLM to SP) for the three rats across all recording sessions. The insets to the right show the *stratum*-dependent median power values computed from the respective points shown in the main plots for both immobile and exploratory periods. A symbol showing a pair of scissors indicates that the specific recording channel was noisy for a majority (≥90%) of the recorded sessions and was discarded from analyses. Wilcox rank sum test *P* values for theta power computed from the identified SLM channel *vs*. SP channel: Rat 1: 2.2×10^{-16} (exp.), 2.2×10^{-16} (imm.); Rat 2: 3.9×10^{-11} (exp.), 2.2×10^{-16} (imm.); Rat 3: 2.2×10^{-16} (exp.), 2.2×10^{-16} (imm.). *A–C* represent average values of theta power in each session, while data points in (*D*) to (*F*) correspond to theta power in single theta epochs. [Colour figure can be viewed at wileyonlinelibrary.com]

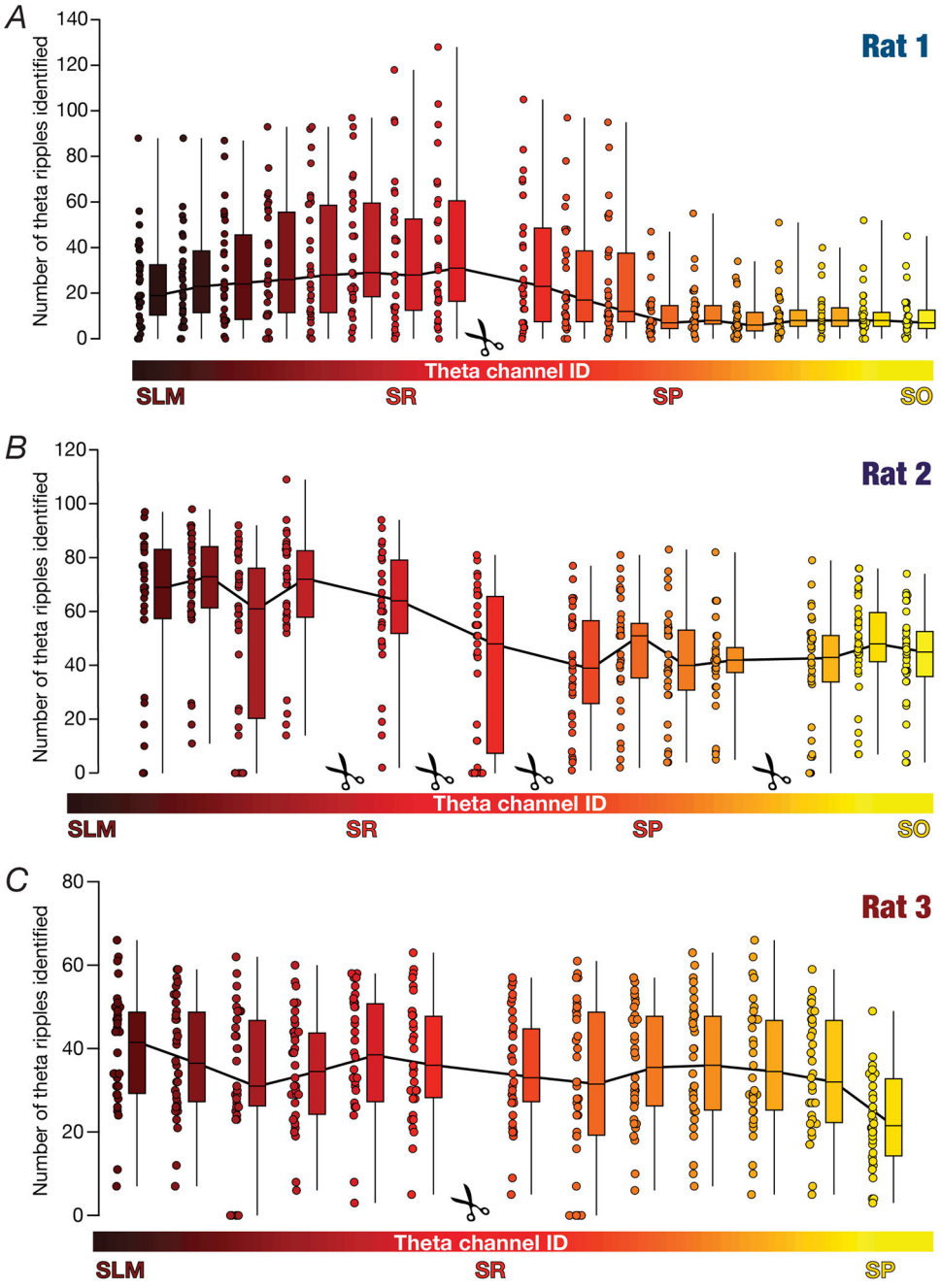

Figure 12. Theta-ripple co-occurrences depended on the channel employed for identifying theta epochs
A–C, the number of theta ripple co-occurrence events are plotted as a function of the identity of the channel from where theta information was derived. Ripples were consistently detected from the identified SP channel for each rat, but theta epoch detection was with reference to each of the different channels spanning all *strata*. The number of theta ripples was computed by counting the number of ripples within theta epochs identified in the chosen theta channel. Each point represents the number of theta ripples identified in each session. The colour code indicates the channel that was used to identify theta epochs. The black rectangles indicate the respective median values and are connected by a thin black line. *A–C*, representing different rats (rats 1–3). A symbol showing a pair of scissors indicates that the specific recording channel was noisy for a majority (≥90%) of the recorded sessions and was discarded from analyses. Wilcox rank sum test *P* values for number of theta ripples identified when the theta channel was SLM *vs*. SP: Rat 1: SLM *vs*. SP: 2.5×10^{-3}; Rat 2: SLM *vs*. SP: 1.9×10^{-7}; Rat 3: SLM *vs*. SP: 1.2×10^{-5}. [Colour figure can be viewed at wileyonlinelibrary.com]

potentials to simultaneously investigate oscillations that are known to manifest differential power distributions across different *strata*. Such multi-electrode acquisition coupled with cross-*strata* analysis of simultaneously recorded oscillatory patterns in two bands unveiled their coexistence, despite the conventional dichotomy that places them to be exclusively prevalent across different behavioural states.

An important design principle in our study is the unbiased nature of the analyses process where there were no implicit assumptions about the dichotomous expression of the oscillatory patterns (theta and ripples) across different behavioural states or across different *strata*. We independently analysed exploratory and immobile states of behaviour, individually assessed all *strata* to identify theta epochs, and placed SP ripples in different groups based on the behavioural state and co-occurrence with theta oscillations. Our analyses clearly confirmed the differential theta profile that is dominant in the SLM and weak in the SP (Fig. 11). This differential power expression implied that the number of detected theta ripples were lesser in number when the SP was used as the theta channel (Fig. 12). These analyses also show that the theta power and the associated *strata*-dependence during immobile periods in the SLM channel was comparable to SLM theta power during awake behaving periods (Fig. 11), together arguing against different sources of theta observed during immobile *vs*. exploratory periods.

Together, our study presents a fundamental design requirement for any analyses pipeline as the need to avoid any assumption regarding one-to-one mapping between behavioural states and oscillatory patterns. Explicitly, the study of theta oscillations and ripples must involve an unbiased analysis pipeline of simultaneously recorded data from multiple *strata*. The absence of multi-*strata* data or the presence of biased assumptions about the exclusive expression of oscillatory bands (e.g. theta band oscillations are observed only in the exploratory periods where the velocity is higher than a large threshold) would result in biased conclusions about the co-occurrence of theta oscillations and ripples. Future studies should not assume the prevalence of theta oscillations to mean exploratory behaviour or vice versa but should instead explicitly account for the differential power profiles of theta-oscillations (predominantly SLM) and ripples (predominantly SP) when analysing behavioural correlates of these oscillatory patterns.

Implications for the co-occurrence of theta oscillations and ripples: future directions

The reported cross-*strata* co-occurrence of theta oscillations with ripples in the CA1 subregion has important behavioural and physiological implications apart from providing several critical avenues for future explorations. The primary implication for the co-occurrence of theta oscillations and ripples is the need to reassess the dichotomy, driven primarily by historic single-*strata* recordings, of theta oscillations and ripples being exclusively associated with preparatory and consummatory behaviours. Such reassessment would also stipulate expansion of the purported roles of ripple-frequency oscillations to theta epochs as well, especially with reference to replay and preplay of neuronal firing sequences within ripples during sleep and awake behavioural states (Csicsvari et al., 2007; Diba & Buzsaki, 2007; Fernandez-Ruiz et al., 2019; Foster & Wilson, 2006; Jadhav et al., 2012; Nokia et al., 2012; O'Neill et al., 2006; Singer et al., 2013). Specifically, sharp wave ripples have been traditionally implicated in consolidation as well as retrieval of memory (Buzsaki, 1989; Buzsaki, 1998; Buzsáki, 2015; Carr et al., 2011; Girardeau & Zugaro, 2011; Girardeau et al., 2009; Joo & Frank, 2018; Qin et al., 1997; Roux et al., 2017; van de Ven et al., 2016; Wu et al., 2017). Our analyses showing co-expression of theta oscillations with ripples add to the growing interest in a role for ripple-frequency oscillations in other awake behaviour including navigational planning, learning and memory-guided decision making (Csicsvari et al., 2007; Diba & Buzsaki, 2007; Fernandez-Ruiz et al., 2019; Foster & Wilson, 2006; Jadhav et al., 2012; Nokia et al., 2012; O'Neill et al., 2006; Singer et al., 2013).

Awake sharp wave ripples and associated replays have been implicated in several functions (Buzsaki, 2015; Fernandez-Ruiz et al., 2019; Gupta et al., 2010; Jadhav et al., 2012; Papale et al., 2016; Tang et al., 2017) with lines of evidence for a relationship of ripple-related activity to task demands (Olafsdottir et al., 2017). In addition, there is evidence for co-occurrence of theta oscillations and ripples during exploratory periods (Csicsvari et al., 2007; O'Neill et al., 2006) and REM sleep (see Buzsaki, 2015 for an example of SPW-R complexes embedded in a stream of theta waves). Importantly, exploratory sharp wave ripples are prevalent in the primate nervous system during visual exploration (Leonard & Hoffman, 2017; Leonard et al., 2015) and there are differences between awake and sleep sharp wave ripples (Csicsvari & Dupret, 2014; Csicsvari et al., 2007; O'Neill et al., 2006). Therefore, an important next step to our report of cross-*strata* co-occurrence of theta-frequency oscillations with ripples during a foraging task is the need to assess such co-occurrence across different behavioural tasks and sleep states. Future studies should explore the prevalence and characteristics of theta ripples across different behavioural states, explicitly assessing cross-dependencies on the task, the novelty of the environment, the state of the animal, pathological conditions, neuromodulatory influences, and within-task switches. Such analyses

should employ simultaneous multi-*strata* recordings coupled with unbiased analyses pipelines that evaluate cross-*strata* signatures of ripples and theta oscillations. In this context, addressing the temporal dynamics of spikes associated with theta ripples across different neurons and associated replays and preplays, especially with specific reference to concurrent theta oscillations in different *strata*, across distinct behavioural states constitutes an important requirement. These questions should be addressed both from the intra- as well as extra-cellular perspectives with somato-dendritic voltage dynamics and cross-*strata* LFPs assessed simultaneously.

The analyses above could expand the potential roles of ripple-frequency oscillations to span the continuum of encoding as well as consolidation, through potential interactions with theta oscillations in the process. Specifically, it is possible that encoding and consolidation processes need not be entirely separated in time and that very brief instances of awake immobility where theta oscillations are also prevalent could potentially engage themselves in both phenomena. In this context, the plateau potentials which have been strongly linked to place-cell formation as well as to sharp waves provide strong links to the processes of consolidation as well as encoding (Bittner et al., 2015; Bittner et al., 2017; Buzsaki, 2015; Dragoi et al., 1999; Fernandez-Ruiz et al., 2019; Jarzebowski et al., 2021; Magee & Grienberger, 2020; McKenzie et al., 2021; O'Neill et al., 2006; O'Neill et al., 2008; Roux et al., 2017; Valero et al., 2022; Vandecasteele et al., 2014). The prevalence of plateau potentials during theta oscillations and their roles in place cell formation (Bittner et al., 2015; Bittner et al., 2017) constitutes an important link, and should be explored with coupled intra- and extra-cellular recordings along the somato-dendritic axis. The role of plateau potentials associated with theta ripples in plasticity as well as place cell emergence, and the question of how they affect hippocampal-cortical interactions during theta *vs*. non-theta ripples are important lines of investigation. Within the realm of plasticity, given the cross-*strata* expression of ripples and theta oscillations, future studies could also explore plasticity associated with cross-pathway interactions between entorhinal and CA3 inputs and their potential role in novelty detection and place cell formation (Basu et al., 2016; Bittner et al., 2017; Magee & Grienberger, 2020; Takahashi & Magee, 2009).

In addition to exploring the prevalence and the physiological roles of co-occurring theta ripples across behavioural states, interventional approaches could be employed to gather direct lines of evidence for the specific roles of theta ripples. For instance, simultaneous detection of SR/SLM theta and ripples in SP, coupled with manipulation of the properties or the prevalence (Aleman-Zapata et al., 2021; Dragoi et al., 1999; Fernandez-Ruiz et al., 2019; Jarzebowski et al., 2021; Karimi Abadchi et al., 2020; Roux et al., 2017; Talakoub et al., 2016; Tingley et al., 2021; Valero et al., 2017; van de Ven et al., 2016; Vandecasteele et al., 2014) of theta ripples (and/or associated theta oscillations) could provide insights about theta ripples in memory encoding, consolidation and storage. The link between the medial septum, a source for theta oscillations to the hippocampal formation (Buzsaki, 2002; Lee et al., 1994), and a metabolic functional role for sharp-wave ripples (Tingley et al., 2021) provides an additional avenue for intervention in exploring the physiological implications of theta ripples. Such interventional experiments should be performed with simultaneous multi-*strata* recordings towards reassessing interactions between medial septum and hippocampal SPW-Rs (Dragoi et al., 1999; Jarzebowski et al., 2021; Vandecasteele et al., 2014), explicitly accounting for theta ripples.

A natural extension for the analyses presented here would be the question of whether such cross-*strata* co-occurrence manifests in the CA3 and the CA2, which play critical roles in the emergence of ripples (Buzsaki, 2015; Chrobak & Buzsaki, 1996; Ylinen et al., 1995) apart from manifesting theta oscillations (Buzsaki, 2002; Colgin, 2013; Goutagny et al., 2009). Furthermore, although our recordings and analyses were limited to the dorsal hippocampus, it is critical to assess co-occurrences with simultaneous multi-*strata* recordings along the dorsoventral and proximo-distal axes of the hippocampus involving brain-wide interactions during such events (Nitzan et al., 2022). Importantly, future studies analyses should assess the intracellular counterparts of theta *vs*. non-theta ripples in the somatic and the dendritic compartments of identified deep *vs*. superficial neurons. It is critical to assess this in a location-dependent fashion as dendritic plateaus might not manifest as somatic depolarization owing to the differential innervation profiles of perisomatic inhibitory neurons onto deep *vs*. superficial neurons (Lee et al., 2014; Sharif et al., 2021; Valero et al., 2015). Thus, simultaneous dendritic recordings could probe the presence of intracellular dendritic plateau potentials and intracellular dendritic theta oscillations during theta ripples identified using multi-*strata* recordings. While these are technically challenging experiments, the availability of multi-electrode recording probes along with high-resolution voltage imaging and other recording techniques in awake behaving animals make such analyses feasible (Abdelfattah et al., 2019; Giocomo, 2015; Steinmetz et al., 2021; Valero et al., 2022; Zong et al., 2022). Such analyses could also assess the role of neurons with basal dendrites that act as axons during theta *vs*. non-theta ripples (Hodapp et al., 2022).

Finally, our focus in the present study was limited to only theta and ripple oscillatory bands. Apart from these, different bands of gamma oscillations are known to play crucial roles in several aspects of hippocampal function

(Bieri et al., 2014; Bragin et al., 1995; Colgin, 2016; Colgin & Moser, 2010; Colgin et al., 2009; Csicsvari et al., 2003; Fernandez-Ruiz et al., 2017; Lisman & Buzsaki, 2008; Lisman & Jensen, 2013; Schomburg et al., 2012; Sullivan et al., 2011; Zheng et al., 2016). Multi-site probes spanning all *strata* should assess cross-*strata* co-occurrence of theta (4–12 Hz), ripple (120–250 Hz), slow gamma (30–60 Hz), medium gamma (60–110 Hz) and fast gamma/epsilon (90–150 Hz) bands of oscillations accounting for their *strata*-specific localization profiles (Fernandez-Ruiz et al., 2017). Specifically, the strong relationship between different bands of gamma oscillations to CA3 and the entorhinal cortex results in *strata*-specific power differences of these bands (Fernandez-Ruiz et al., 2017). Coupled with the co-occurrence of ripples in the *stratum pyramidale* with high theta power in *stratum lacunosum moleculare* reported in this study, the differential spatial prevalence of these different bands of oscillations (theta/ripples/different gamma) offers several exciting routes for cross-*strata* temporal interactions which should be carefully assessed across different awake and sleep states.

References

Abdelfattah, A. S., Kawashima, T., Singh, A., Novak, O., Liu, H., Shuai, Y., Huang, Y.i-C., Campagnola, L., Seeman, S. C., Yu, J., Zheng, J., Grimm, J. B., Patel, R., Friedrich, J., Mensh, B. D., Paninski, L., Macklin, J. J., Murphy, G. J., Podgorski, K., Lin, B.-J., Chen, T.-W., Turner, G. C., Liu, Z., Koyama, M., Svoboda, K., Ahrens, M. B., Lavis, L. D., & Schreiter, E. R. (2019). Bright and photostable chemigenetic indicators for extended in vivo voltage imaging. *Science*, **365**(6454), 699–704.

Aleman-Zapata, A., van der Meij, J., & Genzel, L. (2021). Disrupting ripples: Methods, results, and caveats in closed-loop approaches in rodents. *Journal of Sleep Research*, e13532.

Andersen, P., Morris, R., Amaral, D., Bliss, T., & O'Keefe, J. (2006). *The hippocampus book*. Oxford University Press, New York, USA.

Basu, J., Zaremba, J. D., Cheung, S. K., Hitti, F. L., Zemelman, B. V., Losonczy, A., & Siegelbaum, S. A. (2016). Gating of hippocampal activity, plasticity, and memory by entorhinal cortex long-range inhibition. *Science*, **351**(6269), aaa5694.

Bieri, K. W., Bobbitt, K. N., & Colgin, L. L. (2014). Slow and fast gamma rhythms coordinate different spatial coding modes in hippocampal place cells. *Neuron*, **82**(3), 670–681.

Bittner, K. C., Grienberger, C., Vaidya, S. P., Milstein, A. D., Macklin, J. J., Suh, J., Tonegawa, S., & Magee, J. C. (2015). Conjunctive input processing drives feature selectivity in hippocampal CA1 neurons. *Nature Neuroscience*, **18**(8), 1133–1142.

Bittner, K. C., Milstein, A. D., Grienberger, C., Romani, S., & Magee, J. C. (2017). Behavioral time scale synaptic plasticity underlies CA1 place fields. *Science*, **357**(6355), 1033–1036.

Bragin, A., Jando, G., Nadasdy, Z., Hetke, J., Wise, K., & Buzsaki, G. (1995). Gamma (40-100 Hz) oscillation in the hippocampus of the behaving rat. *Journal of Neuroscience*, **15**(1), 47–60.

Buzsáki, G. (1989). Two-stage model of memory trace formation: A role for "noisy" brain states. *Neuroscience*, **31**(3), 551–570.

Buzsák, G. (1998). Memory consolidation during sleep: A neurophysiological perspective. *Journal of Sleep Research*, **7(Suppl** S1), 17–23.

Buzsáki, G. (2002). Theta oscillations in the hippocampus. *Neuron*, **33**(3), 325–340.

Buzsáki, G. (2015). Hippocampal sharp wave-ripple: A cognitive biomarker for episodic memory and planning. *Hippocampus*, **25**(10), 1073–1188.

Buzsáki, G., Lai-Wo, S. L., & Vanderwolf, C. H. (1983). Cellular bases of hippocampal EEG in the behaving rat. *Brain Research Reviews*, **6**(2), 139–171.

Carr, M. F., Jadhav, S. P., & Frank, L. M. (2011). Hippocampal replay in the awake state: A potential substrate for memory consolidation and retrieval. *Nature Neuroscience*, **14**(2), 147–153.

Chrobak, J. J., & Buzsáki, G. (1996). High-frequency oscillations in the output networks of the hippocampal-entorhinal axis of the freely behaving rat. *Journal of Neuroscience*, **16**(9), 3056–3066.

Colgin, L. L. (2013). Mechanisms and functions of theta rhythms. *Annual Review of Neuroscience*, **36**(1), 295–312.

Colgin, L. L. (2016). Rhythms of the hippocampal network. *Nature Reviews Neuroscience*, **17**(4), 239–249.

Colgin, L. L., Denninger, T., Fyhn, M., Hafting, T., Bonnevie, T., Jensen, O., Moser, M.-B., & Moser, E. I. (2009). Frequency of gamma oscillations routes flow of information in the hippocampus. *Nature*, **462**(7271), 353–357.

Colgin, L. L., & Moser, E. I. (2010). Gamma oscillations in the hippocampus. *Physiology*, **25**(5), 319–329.

Csicsvari, J., & Dupret, D. (2014). Sharp wave/ripple network oscillations and learning-associated hippocampal maps. *Philosophical Transactions of the Royal Society of London-Series B: Biological Sciences*, **369**(1635), 20120528.

Csicsvari, J., Jamieson, B., Wise, K. D., & Buzsáki, G. (2003). Mechanisms of gamma oscillations in the hippocampus of the behaving rat. *Neuron*, **37**(2), 311–322.

Csicsvari, J., O'neill, J., Allen, K., & Senior, T. (2007). Place-selective firing contributes to the reverse-order reactivation of CA1 pyramidal cells during sharp waves in open-field exploration. *The European Journal of Neuroscience*, **26**(3), 704–716.

Diba, K., & Buzsáki, G. (2007). Forward and reverse hippocampal place-cell sequences during ripples. *Nature Neuroscience*, **10**(10), 1241–1242.

Dragoi, G., Carpi, D., Recce, M., Csicsvari, J., & Buzsáki, G. (1999). Interactions between hippocampus and medial septum during sharp waves and theta oscillation in the behaving rat. *Journal of Neuroscience*, **19**(14), 6191–6199.

Epsztein, J., Brecht, M., & Lee, A. K. (2011). Intracellular determinants of hippocampal CA1 place and silent cell activity in a novel environment. *Neuron*, **70**(1), 109–120.

Fernández-Ruiz, A., Oliva, A., Fermino De Oliveira, E., Rocha-Almeida, F., Tingley, D., & Buzsáki, G. (2019). Long-duration hippocampal sharp wave ripples improve memory. *Science*, **364**(6445), 1082–1086.

Fernández-Ruiz, A., Oliva, A., Nagy, G. A., Maurer, A. P., Berényi, A., & Buzsáki, G. (2017). Entorhinal-CA3 dual-input control of spike timing in the hippocampus by theta-gamma coupling. *Neuron*, **93**(5), 1213–1226.e5.

Foster, D. J., & Wilson, M. A. (2006). Reverse replay of behavioural sequences in hippocampal place cells during the awake state. *Nature*, **440**(7084), 680–683.

Giocomo, L. M. (2015). Large scale in vivo recordings to study neuronal biophysics. *Current Opinion in Neurobiology*, **32**, 1–7.

Girardeau, G., Benchenane, K., Wiener, S. I., Buzsáki, G., & Zugaro, M. B. (2009). Selective suppression of hippocampal ripples impairs spatial memory. *Nature Neuroscience*, **12**(10), 1222–1223.

Girardeau, G., & Lopes-Dos-Santos, V. (2021). Brain neural patterns and the memory function of sleep. *Science*, **374**(6567), 560–564.

Girardeau, G., & Zugaro, M. (2011). Hippocampal ripples and memory consolidation. *Current Opinion in Neurobiology*, **21**(3), 452–459.

Gordon, J. A., Lacefield, C. O., Kentros, C. G., & Hen, R. (2005). State-dependent alterations in hippocampal oscillations in serotonin 1A receptor-deficient mice. *Journal of Neuroscience*, **25**(28), 6509–6519.

Goutagny, R., Jackson, J., & Williams, S. (2009). Self-generated theta oscillations in the hippocampus. *Nature Neuroscience*, **12**(12), 1491–1493.

Gupta, A. S., Van Der Meer, M. A. A., Touretzky, D. S., & Redish, A. D. (2010). Hippocampal replay is not a simple function of experience. *Neuron*, **65**(5), 695–705.

Hasselmo, M. E., & Stern, C. E. (2014). Theta rhythm and the encoding and retrieval of space and time. *Neuroimage*, **85(Pt** 2), 656–666.

Hodapp, A., Kaiser, M. E., Thome, C., Ding, L., Rozov, A., Klumpp, M., Stevens, N., Stingl, M., Sackmann, T., Lehmann, N., Draguhn, A., Burgalossi, A., Engelhardt, M., & Both, M. (2022). Dendritic axon origin enables information gating by perisomatic inhibition in pyramidal neurons. *Science*, **377**(6613), 1448–1452.

Jadhav, S. P., Kemere, C., German, P. W., & Frank, L. M. (2012). Awake hippocampal sharp-wave ripples support spatial memory. *Science*, **336**(6087), 1454–1458.

Jarzebowski, P., Tang, C. S., Paulsen, O., & Hay, Y. A. (2021). Impaired spatial learning and suppression of sharp wave ripples by cholinergic activation at the goal location. *Elife*, **10**.

Joo, H. R., & Frank, L. M. (2018). The hippocampal sharp wave-ripple in memory retrieval for immediate use and consolidation. *Nature reviews Neuroscience*, **19**(12), 744–757.

Kamondi, A., Acsády, L., & Buzsáki, G. (1998). Dendritic spikes are enhanced by cooperative network activity in the intact hippocampus. *Journal of Neuroscience*, **18**(10), 3919–3928.

Kamondi, A., Acsády, L., Wang, X.-J., & Buzsáki, G. (1998). Theta oscillations in somata and dendrites of hippocampal pyramidal cells in vivo: Activity-dependent phase-precession of action potentials. *Hippocampus*, **8**(3), 244–261.

Karimi Abadchi, J., Nazari-Ahangarkolaee, M., Gattas, S., Bermudez-Contreras, E., Luczak, A., Mcnaughton, B. L., & Mohajerani, M. H. (2020). Spatiotemporal patterns of neocortical activity around hippocampal sharp-wave ripples. *Elife*, **9**.

Klausberger, T., Magill, P. J., Márton, L. F., Roberts, J. D. B., Cobden, P. M., Buzsáki, G., & Somogyi, P. (2003). Brain-state- and cell-type-specific firing of hippocampal interneurons in vivo. *Nature*, **421**(6925), 844–848.

Lee, M. G., Chrobak, J. J., Sik, A., Wiley, R. G., & Buzsáki, G. (1994). Hippocampal theta activity following selective lesion of the septal cholinergic system. *Neuroscience*, **62**(4), 1033–1047.

Lee, S.-H., Marchionni, I., Bezaire, M., Varga, C., Danielson, N., Lovett-Barron, M., Losonczy, A., & Soltesz, I. (2014). Parvalbumin-positive basket cells differentiate among hippocampal pyramidal cells. *Neuron*, **82**(5), 1129–1144.

Leonard, T. K., & Hoffman, K. L. (2017). Sharp-wave ripples in primates are enhanced near remembered visual objects. *Current Biology : CB*, **27**(2), 257–262.

Leonard, T. K., Mikkila, J. M., Eskandar, E. N., Gerrard, J. L., Kaping, D., Patel, S. R., Womelsdorf, T., & Hoffman, K. L. (2015). Sharp wave ripples during visual exploration in the primate hippocampus. *Journal of Neuroscience*, **35**(44), 14771–14782.

Lisman, J., & Buzsaki, G. (2008). A neural coding scheme formed by the combined function of gamma and theta oscillations. *Schizophrenia Bulletin*, **34**(5), 974–980.

Lisman, J. E., & Jensen, O. (2013). The theta-gamma neural code. *Neuron*, **77**(6), 1002–1016.

Lopes, G. A., Bonacchi, N., Frazão, J., Neto, J. P., Atallah, B. V., Soares, S., Moreira, L.-S., Matias, S., Itskov, P. M., Correia, P.-C. A., Medina, R. E., Calcaterra, L., Dreosti, E., Paton, J. J., & Kampff, A. R. (2015). Bonsai: An event-based framework for processing and controlling data streams. *Frontiers in Neuroinformatics*, **9**, 7.

Magee, J. C., & Grienberger, C. (2020). Synaptic plasticity forms and functions. *Annual Review of Neuroscience*, **43**(1), 95–117.

Marder, E., & Taylor, A. L. (2011). Multiple models to capture the variability in biological neurons and networks. *Nature Neuroscience*, **14**(2), 133–138.

Mckenzie, S., Huszár, R., English, D. F., Kim, K., Christensen, F., Yoon, E., & Buzsáki, G. (2021). Preexisting hippocampal network dynamics constrain optogenetically induced place fields. *Neuron*, **109**(6), 1040–1054.e7.e1047.

Milstein, A. D., Li, Y., Bittner, K. C., Grienberger, C., Soltesz, I., Magee, J. C., & Romani, S. (2021). Bidirectional synaptic plasticity rapidly modifies hippocampal representations. *Elife*, **10**, e73046.

Mizuseki, K., Diba, K., Pastalkova, E., & Buzsáki, G. (2011). Hippocampal CA1 pyramidal cells form functionally distinct sublayers. *Nature Neuroscience*, **14**(9), 1174–1181.

Navas-Olive, A., Amaducci, R., Jurado-Parras, M.-T., Sebastian, E. R., & De La Prida, L. M. (2022). Deep learning based feature extraction for prediction and interpretation of sharp-wave ripples in the rodent hippocampus. *Elife*, **11**.

Nitzan, N., Swanson, R., Schmitz, D., & Buzsáki, G. (2022). Brain-wide interactions during hippocampal sharp wave ripples. *The Proceedings of the National Academy of Sciences*, **119**(20), e2200931119.

Nokia, M. S., Mikkonen, J. E., Penttonen, M., & Wikgren, J. (2012). Disrupting neural activity related to awake-state sharp wave-ripple complexes prevents hippocampal learning. *Frontiers in Behavioral Neuroscience*, **6**, 84.

O'neill, J., Senior, T., & Csicsvari, J. (2006). Place-selective firing of CA1 pyramidal cells during sharp wave/ripple network patterns in exploratory behavior. *Neuron*, **49**(1), 143–155.

O'neill, J., Senior, T. J., Allen, K., Huxter, J. R., & Csicsvari, J. (2008). Reactivation of experience-dependent cell assembly patterns in the hippocampus. *Nature Neuroscience*, **11**(2), 209–215.

Ólafsdóttir, H. F., Carpenter, F., & Barry, C. (2017). Task demands predict a dynamic switch in the content of awake hippocampal replay. *Neuron*, **96**(4), 925–935.e6 e926.

Papale, A. E., Zielinski, M. C., Frank, L. M., Jadhav, S. P., & Redish, A. D. (2016). Interplay between hippocampal sharp-wave-ripple events and vicarious trial and error behaviors in decision making. *Neuron*, **92**(5), 975–982.

Qin, Y.u-L., Mcnaughton, B. L., Skaggs, W. E., & Barnes, C. A. (1997). Memory reprocessing in corticocortical and hippocampocortical neuronal ensembles. *Philosophical Transactions of the Royal Society of London-Series B: Biological Sciences*, **352**(1360), 1525–1533.

R Core Team (2013). *R: A Language and Environment for Statistical Computing*. R Foundation for Statistical Computing (http://www.R-project.org), Vienna, Austria.

Rathour, R. K., & Narayanan, R. (2019). Degeneracy in hippocampal physiology and plasticity. *Hippocampus*, **29**(10), 980–1022.

Roumis, D. K., & Frank, L. M. (2015). Hippocampal sharp-wave ripples in waking and sleeping states. *Current Opinion in Neurobiology*, **35**, 6–12.

Roux, L., Hu, B.o, Eichler, R., Stark, E., & Buzsáki, G. (2017). Sharp wave ripples during learning stabilize the hippocampal spatial map. *Nature Neuroscience*, **20**(6), 845–853.

Schomburg, E. W., Anastassiou, C. A., Buzsáki, G., & Koch, C. (2012). The spiking component of oscillatory extracellular potentials in the rat hippocampus. *Journal of Neuroscience*, **32**(34), 11798–11811.

Sharif, F., Tayebi, B., Buzsáki, G., Royer, S., & Fernandez-Ruiz, A. (2021). Subcircuits of deep and superficial CA1 place cells support efficient spatial coding across heterogeneous environments. *Neuron*, **109**(2), 363–376.e6 e366.

Singer, A. C., Carr, M. F., Karlsson, M. P., & Frank, L. M. (2013). Hippocampal SWR activity predicts correct decisions during the initial learning of an alternation task. *Neuron*, **77**(6), 1163–1173.

Sinha, M., & Narayanan, R. (2022). Active dendrites and local field potentials: Biophysical mechanisms and computational explorations. *Neuroscience*, **489**, 111–142.

Steinmetz, N. A., Aydin, C., Lebedeva, A., Okun, M., Pachitariu, M., Bauza, M., Beau, M., Bhagat, J., Böhm, C., Broux, M., Chen, S., Colonell, J., Gardner, R. J., Karsh, B., Kloosterman, F., Kostadinov, D., Mora-Lopez, C., O'callaghan, J., Park, J., … Harris, T. D. (2021). Neuropixels 2.0: A miniaturized high-density probe for stable, long-term brain recordings. *Science*, **372**(6539),

Sullivan, D., Csicsvari, J., Mizuseki, K., Montgomery, S., Diba, K., & Buzsaki, G. (2011). Relationships between hippocampal sharp waves, ripples, and fast gamma oscillation: influence of dentate and entorhinal cortical activity. *Journal of Neuroscience*, **31**(23), 8605–8616.

Takahashi, H., & Magee, J. C. (2009). Pathway interactions and synaptic plasticity in the dendritic tuft regions of CA1 pyramidal neurons. *Neuron*, **62**(1), 102–111.

Talakoub, O., Gomez Palacio Schjetnan, A., Valiante, T. A., Popovic, M. R., & Hoffman, K. L. (2016). Closed-loop interruption of hippocampal ripples through fornix stimulation in the non-human primate. *Brain Stimulation*, **9**(6), 911–918.

Tang, W., Shin, J. D., Frank, L. M., & Jadhav, S. P. (2017). Hippocampal-prefrontal reactivation during learning is stronger in awake compared with sleep states. *Journal of Neuroscience*, **37**(49), 11789–11805.

Thomson, D. J. (1982). Spectrum estimation and harmonic-analysis. *Proceedings of the Institute of Electrical and Electronics Engineers*, **70**(9), 1055–1096.

Tingley, D., Mcclain, K., Kaya, E., Carpenter, J., & Buzsáki, G. (2021). A metabolic function of the hippocampal sharp wave-ripple. *Nature*, **597**(7874), 82–86.

Valero, M., Averkin, R. G., Fernandez-Lamo, I., Aguilar, J., Lopez-Pigozzi, D., Brotons-Mas, J. R., Cid, E., Tamas, G., & Menendez De La Prida, L. (2017). Mechanisms for selective single-cell reactivation during offline sharp-wave ripples and their distortion by fast ripples. *Neuron*, **94**(6), 1234–1247.e7.

Valero, M., Cid, E., Averkin, R. G., Aguilar, J., Sanchez-Aguilera, A., Viney, T. J., Gomez-Dominguez, D., Bellistri, E., & De La Prida, L. M. (2015). Determinants of different deep and superficial CA1 pyramidal cell dynamics during sharp-wave ripples. *Nature Neuroscience*, **18**(9), 1281–1290.

Valero, M., Zutshi, I., Yoon, E., & Buzsáki, G. (2022). Probing subthreshold dynamics of hippocampal neurons by pulsed optogenetics. *Science*, **375**(6580), 570–574.

Van De Ven, G. M., Trouche, S., Mcnamara, C. G., Allen, K., & Dupret, D. (2016). Hippocampal offline reactivation consolidates recently formed cell assembly patterns during sharp wave-ripples. *Neuron*, **92**(5), 968–974.

Vandecasteele, M., Varga, V., Berényi, A., Papp, E., Barthó, P., Venance, L., Freund, T. F., & Buzsáki, G. (2014). Optogenetic activation of septal cholinergic neurons suppresses sharp wave ripples and enhances theta oscillations in the hippocampus. *Proceedings of the National Academy of Sciences*, **111**(37), 13535–13540.

Wu, C.-T., Haggerty, D., Kemere, C., & Ji, D. (2017). Hippocampal awake replay in fear memory retrieval. *Nature Neuroscience*, **20**(4), 571–580.
Ylinen, A., Bragin, A., Nadasdy, Z., Jando, G., Szabo, I., Sik, A., & Buzsaki, G. (1995). Sharp wave-associated high-frequency oscillation (200 Hz) in the intact hippocampus: network and intracellular mechanisms. *Journal of Neuroscience*, **15**(1), 30–46.
Zhao, X., Wang, Y., Spruston, N., & Magee, J. C. (2020). Membrane potential dynamics underlying context-dependent sensory responses in the hippocampus. *Nature Neuroscience*, **23**(7), 881–891.
Zheng, C., Bieri, K. W., Hsiao, Y.i-T., & Colgin, L. L. (2016). Spatial sequence coding differs during slow and fast gamma rhythms in the hippocampus. *Neuron*, **89**(2), 398–408.
Zong, W., Obenhaus, H. A., Skytøen, E. R., Eneqvist, H., De Jong, N. L., Vale, R., Jorge, M. R., Moser, M.-B., & Moser, E. I. (2022). Large-scale two-photon calcium imaging in freely moving mice. *Cell*, **185**(7), 1240–1256.e30 e1230.
Zutshi, I., Valero, M., Fernández-Ruiz, A., & Buzsáki, G. (2022). Extrinsic control and intrinsic computation in the hippocampal CA1 circuit. *Neuron*, **110**(4), 658–673.e5 e655.

Additional information

Data availability statement

All data and analyses required for assessment of this manuscript are available as part of the figures, tables and statistical summary files. Additional supplementary files are available along with the preprint version of this manuscript at https://doi.org/10.1101/2022.11.15.516579.

Competing interests

The authors declare that they have no competing interests.

Author contributions

P.S., R.B. and R.N. designed experiments. P.S. and R.B. performed experiments. P.S. analysed data. P.S. and R.N. wrote the paper with inputs from R.B.

Funding

Wellcome Trust DBT India Alliance (India Alliance): Rishikesh, Narayanan, IA/S/16/2/502 727; University Grants Commission (UGC): Reshma Basak, Scholarship; Ministry of Education, India (MoE): Pavithraa, Seenivasan, Scholarship.

Acknowledgements

We thank members of the cellular neurophysiology laboratory for helpful discussions and for comments on a draft of this manuscript. We thank Dr Sachin Deshmukh, Indraja Jakhalekar, Sriram Narayanan and Dr Sunandha Srikanth for helpful advice and feedback through different stages of the study. We thank Dr Liset de la Prida for analysis advice and helpful comments. This work was supported by the DBT-Wellcome Trust India Alliance (Senior fellowship to RN: IA/S/16/2/502727), the University Grants Commission (RB) and the ministry of education (PS).

Keywords

hippocampus, *in vivo* recordings, local field potential, ripples, theta oscillations

Supporting information

Additional supporting information can be found online in the Supporting Information section at the end of the HTML view of the article. Supporting information files available:

Statistical Summary Document
Peer Review History